

Review

Surface Laser Treatment of Cast Irons: A Review

Néstor Catalán ^{1,*} , Esteban Ramos-Moore ^{2,3}, Adrian Boccardo ^{4,5,6}  and Diego Celentano ^{1,3,*} 

- ¹ Departamento de Ingeniería Mecánica y Metalúrgica, Pontificia Universidad Católica de Chile, Av. Vicuña Mackenna 4860, Macul, Santiago 7820436, Chile
- ² Laboratorio de Películas Delgadas UC, Instituto de Física, Pontificia Universidad Católica de Chile, Casilla 306, Av. Vicuña Mackenna 4860, Macul, Santiago 7820436, Chile; evramos@uc.cl
- ³ Centro de Investigación en Nanotecnología y Materiales Avanzados (CIEN-UC), Pontificia Universidad Católica de Chile, Av. Vicuña Mackenna 4860, Macul, Santiago 7820436, Chile
- ⁴ Mechanical Engineering, School of Engineering, College of Science and Engineering, National University of Ireland (NUI), University Road, H91 HX31 Galway, Ireland; adrian.boccardo@nuigalway.ie
- ⁵ I-Form Advanced Manufacturing Research Centre, NUI, University Road, H91 HX31 Galway, Ireland
- ⁶ Instituto de Estudios Avanzados en Ingeniería y Tecnología (IDIT), CONICET-Universidad Nacional de Córdoba, Vélez Sarsfield 1611, Córdoba X5000, Argentina
- * Correspondence: nacatalan@uc.cl (N.C.); dcelentano@ing.puc.cl (D.C.)

Abstract: Heat treatments are frequently used to modify the microstructure and mechanical properties of materials according to the requirements of their applications. Laser surface treatment (LST) has become a relevant technique due to the high control of the parameters and localization involved in surface modification. It allows for the rapid transformation of the microstructure near the surface, resulting in minimal distortion of the workpiece bulk. LST encompasses, in turn, laser surface melting and laser surface hardening techniques. Many of the works devoted to studying the effects of LST in cast iron are diverse and spread in several scientific communities. This work aims to review the main experimental aspects involved in the LST treatment of four cast-iron groups: gray (lamellar) cast iron, pearlitic ductile (nodular) iron, austempered ductile iron, and ferritic ductile iron. The effects of key experimental parameters, such as laser power, scanning velocity, and interaction time, on the microstructure, composition, hardness, and wear are presented, discussed, and overviewed. Finally, we highlight the main scientific and technological challenges regarding LST applied to cast irons.

Keywords: laser treatment; cast irons; microstructure; mechanical properties; wear



Citation: Catalán, N.; Ramos-Moore, E.; Boccardo, A.; Celentano, D. Surface Laser Treatment of Cast Irons: A Review. *Metals* **2022**, *12*, 562. <https://doi.org/10.3390/met12040562>

Academic Editor: Sergey N. Grigoriev

Received: 16 February 2022

Accepted: 24 March 2022

Published: 26 March 2022

Publisher's Note: MDPI stays neutral with regard to jurisdictional claims in published maps and institutional affiliations.



Copyright: © 2022 by the authors. Licensee MDPI, Basel, Switzerland. This article is an open access article distributed under the terms and conditions of the Creative Commons Attribution (CC BY) license (<https://creativecommons.org/licenses/by/4.0/>).

1. Introduction

Over the last few decades, cast irons have been widely used in a variety of applications, such as for shafts, axles, engines, and gears in automobile parts or general industrial machinery [1–4], due to their high machinability, good mechanical properties, and low cost compared to other alloys.

Because of the increased production volume, an exhaustive characterization of the mechanical properties and fatigue behavior of cast irons has been extensively reported in the past literature. In addition, several tribological studies have been performed to address the wear mechanisms under diverse sliding conditions, as well as to establish a comparison of their wear rates against other industrial materials.

In general, intense loads in sliding tests reveal higher wear rates in cast irons than in steels. Thus, in extreme wear applications, e.g., mining, marine, aeronautic, or military industries, it is frequently required to improve their hardness and wear resistance in critical points of the material to meet requirements related to corrosion or fracture/fatigue failures. For this purpose, many conventional treatments have been developed and implemented to enhance the performance of cast irons in specific applications. Nonetheless, these techniques usually involve a full transformation of the workpiece, altering many of its beneficial bulk properties.

In this context, laser surface treatment (LST) has emerged as a novel opportunity to improve the useful life of cast irons. This technique is characterized by a precise, clean, and fast thermal process, where the heat input from a laser beam raises the temperature at the surface of the specimen, and then it is rapidly conducted into the rest of the material. The objective of LST is to achieve temperatures above the point of critical transformation (austenitization or melting temperature), following a self-quenching process from the unaffected case bulk. Depending on the cooling and solidification rates to which they are exposed during the treatment, new phases can arise, directly influencing the new mechanical properties of the material.

Past articles and reviews have addressed, in general terms, the benefits and challenges of LST of a variety of cast irons. However, a thorough comparison and analysis of the importance of the initial microstructure and laser properties is yet to be performed. Therefore, this article presents a review of the literature according to LST of industrial iron castings, in order to understand the similarities and differences associated with these parameters and to serve as a guide to a reliable implementation and optimization of this technique.

First, a brief description of typical cast irons is provided, highlighting the different morphologies and conventional heat treatments that are commonly conducted in each one. Secondly, a more detailed theoretical basis of LST is presented, along with a summary of standard laser configurations used in metallic surface treatments, i.e., laser type, power, and scanning velocity. Moreover, the influence of other advanced parameters in the efficiency of LST is remarked. Afterward, an exploration of the results obtained in LST of gray cast irons (GIs) is offered to establish the influence of graphite morphology on the microstructural transformations that the treatment induces, as well as the resulting properties of the samples. Then the most relevant works for ductile irons (DIs) with predominantly pearlitic matrices are exposed, emphasizing the results as a function of laser configurations and characterization tests. Subsequently, investigations on laser-modified austempered ductile iron (ADI) castings are reviewed, mainly highlighting the differences in the scope of the treatment in terms of hardness, wear resistance, and depth of the affected area. Articles dealing with ferritic nodular cast iron treatments are then presented, addressing the main challenges of transforming the microstructure without melting the original matrix. To complete the review, a discussion of LST across all types of cast irons is given, highlighting the differences in achieved microstructure, hardness, and wear-related properties as a function of base material and laser operating parameters. At the same time, the main advantages and limitations of the treatments are presented, noting the improvement in overall performance compared to as-cast specimens. Finally, future technological, economic, and investigation areas related to the LST of cast irons are suggested.

2. Cast Irons

Cast irons comprise a large family of solid ferrous alloys. The main difference with steels is the higher carbon (C) and silicon (Si) content, with the richer carbon phase being critical in the microstructural transformations of the matrix. Additionally, significant amounts of manganese (Mn), phosphorus (P), and sulfur (S), as well as minor contents of molybdenum (Mo), chromium (Cr), and nickel (Ni), can be found in these castings. The most common classification for cast irons is based on microstructural features. The first feature is graphite morphology, where cast irons can be classified mainly as lamellar (gray) or nodular (spheroidal or ductile). On the other hand, the matrix phase can be used to identify cast irons as ferritic, pearlitic, martensitic, austenitic, or bainitic [5].

GIs are a broad class of casting alloys characterized by a lamellar (flake) graphite disposal, usually in a ferrous matrix. They are traditionally used in industrial applications, due to their good castability, flexible mechanical properties, and low cost compared to steel [6,7]. A variety of fatigue and crack growth models have been performed [8–10] to predict the fatigue life of GIs in standard applications, while other tribological studies [11–16] have identified the main wear mechanisms under dry and lubricated conditions, emphasizing the high variability in wear rates in different tribo-systems. Graphite plays a

major lubricating role that helps reduce the wear coefficient. However, a cracking tendency is observed under high loads, and adhesion is the main wear mechanism in lubricated environments.

On the other hand, DI is a ferrous material containing graphite in a small and rounded shape, due to the nodulizing effect of magnesium, and it is present in higher concentrations. In comparison, DI exhibits higher strength and ductility, which is the main reason for its growth in industrial applications [5]. The effects of cooling rate and matrix type (i.e., pearlitic/ferritic) on the mechanical properties of DIs have been explored both experimentally and numerically [17–22], figuring that an increment of the ferritic or pearlitic phase can lead to very dissimilar properties. Thus, an appropriate balance of the alloying elements and the initial microstructure is needed to achieve the desired performance. In this regard, studies on crack growth have been conducted [23,24] that show a comparable behavior to that of GIs. However, under similar conditions, DI presents better fatigue resistance due to the higher stress intensity factor and the nodular shape of graphite that blunts the crack, while the lamellar shape of GI exhibits an anisotropic behavior that leads to stress concentrations at the interface between the matrix and the flake tips. Furthermore, wear analyses of DIs have been carried out to understand the underlying wear mechanisms and to compare the removal rates with those of industrial steels [4,25–28]. In mild wear environments, plowing is the predominant wear mechanism, and as the load applied increases, sliding wear becomes more severe, due to enhancement of the plastic deformation and initiation of cracks in the subsurface. Moreover, the influence of both bulk and matrix microhardness in the wear rates of ferrous alloys has been addressed, revealing that some initial cast irons microstructures could lead to tribological performances in the range of soft industrial steels, e.g., 52,100 and 1070.

Over the last decades, austempered ductile cast iron (ADI) has emerged as a novel option for achieving a good combination of mechanical properties. Because of its low cost and good machinability, ADIs have gained more interest in automotive and agricultural applications [2,3,29]. The characteristic ausferritic matrix is achieved by a pre-heating cycle, whose quality is primarily influenced by the processing window [30], i.e., the time interval between the ausferritic transformation and the carbide precipitation (Figure 1). Additional modifications of the austempering process have been explored to enhance the mechanical properties of ADIs [31,32].

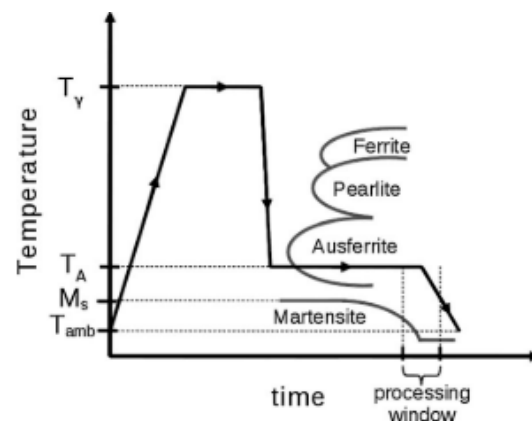


Figure 1. Phase transformations and variables of a conventional austempering heat treatment (Reprinted with permission from ref. [30]. 2015 Springer Nature).

The main limitations of ADI are its lower machinability and ductility when compared to as-cast ductile iron, due to higher austenitic content and the absence of pro-eutectoid ferrite, responsible for the work hardening of the material [29]. Nonetheless, tribological studies have demonstrated a superior ADI wear resistance in comparison to both GI and DI [33]. This difference is attributed to the higher toughness achieved by the bainitic microstructure of ADI, as it leads to severe plastic deformation in the direction of sliding

with minimum material loss. Moreover, wear resistance can be further enhanced in ADIs based in the pre-austempered iron matrix, as graphite morphology plays a significant role in the control of crack propagation and thermal conductivity of the material and, therefore, of its thermal fatigue resistance.

Alternatively, the improvement of mechanical properties to fulfill industrial requirements has been achieved by applying conventional heat treatments on as-cast iron samples that can modify their entire primary microstructure. The most common treatments consist of normalizing, annealing, or quench-tempering, where furnaces are operated to provide uniform heating through the metallic piece until a critical temperature is reached, since, in the absence of chromium, iron carbides can be dissociated into austenite and graphite at annealing temperatures [34]. The microstructural transformations are also influenced by the cooling rate, which varies with the selected treatment.

The main results of normalizing are the enhancement of different properties, such as hardness, impact toughness, and tensile strength, and can be optimized with selected temperature, holding time, and cooling rate [35]. If the goal is to achieve high ductility and machinability at the expense of strength, then full annealing is conducted. The matrix transformations include the removal of cementite and decomposition of pearlite into graphite and ferrite [36]. Quench-tempering is used to mostly improve the wear resistance and strength of cast irons. The resulting microstructure of GIs consists of a retained austenite matrix with carbon-saturated martensite plates that becomes finer with higher alloying elements content [37], while a primary martensitic structure with small soft ferrite regions adjacent to the graphite nodules can be achieved in DIs [38].

3. Laser Processing of Cast Irons

As reviewed in the previous section, conventional heat treating of cast irons has been extensively used to enhance their performance to higher standards. However, it has been acknowledged that altering the properties of the entire bulk, e.g., to achieve a hardening effect, can be detrimental to the machinability advantages of these materials. Therefore, LST has appeared as a major opportunity to efficiently improve the overall performance of cast irons.

This technique is characterized by a highly localized, chemically clean, automatable, and fast thermal process, where only controlled regions of the material are hardened during the treatment. Steen and Mazumder [39] extensively detail the theoretical basis of LST, in which a laser beam is defocused or oscillated to irradiate a small area with high power density, and the relative motion between the beam and the sample, usually provided by a CNC table, allows users to precisely cover complex geometries (Figure 2). The laser heat supply raises the temperature at the surface of the specimen, which is transferred into the metallic body by thermal conduction.

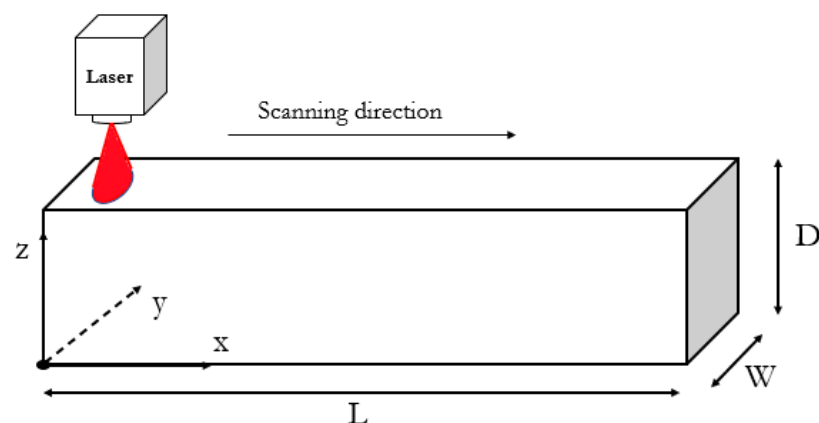


Figure 2. Schematic representation of LST in rectangular samples.

The objective of LST is to achieve temperatures above the point of critical transformation, which is the austenitizing temperature (solid-state transformation) in the case of laser surface hardening (LSH), or the melting temperature in the case of laser surface melting (LSM). Then a rapid self-quenching process takes place, because of the large volume of adjacent and unaffected material, resulting in a controlled low distortion of the workpiece. Since the heating rates are very high, the initial transformations take place under conditions far from equilibrium, while phase transformations on cooling can be addressed with the help of suitable continuous cooling transformation (CCT) diagrams. Depending on the cooling and solidification rates to which they are exposed during the treatment, the final microstructure directly influences the new mechanical properties of the material.

Laser surface modification of metallic samples, including cast irons, has been performed for over fifty years. As one of the first available tools, CO₂ lasers have been widely employed to achieve both LSH and LSM, usually aided by the application of a thin coating, in order to ensure higher absorption and thermal efficiency. However, modern breakthroughs have allowed the use of more efficient lasers for these purposes, such as Nd:YAG and diode lasers, where LST has been carried out with and without coatings with successful results. As shown in Table 1, other LST features include setting an appropriate scanning velocity, the laser power distribution, spot geometry and size, the number of scanned tracks (with or without overlapping), and the use of shielding gas to prevent oxidation. As some authors define, the linear energy density (or heat input) is a global parameter that includes the effect of both laser power and scanning speed by the following expression:

$$\bar{E} = \frac{P}{v}, \quad (1)$$

where \bar{E} is the heat input, P is the laser power, and v is the scanning velocity. In circular spots, this definition can be modified to consider the geometry of the irradiation zone and the energy distribution.

Table 1. Typical parameters and characterization tests used in LST of cast irons.

LST Parameter	Regular Value/Selection
Laser type	CO ₂ , Nd:YAG, fiber (diode)
Coating (optional)	Graphite, manganese/zinc phosphate
Shielding gas (optional)	Argon, nitrogen, helium
Laser power	Fixed, PID controller, linear ramp
Power distribution	Gaussian, uniform
Laser scanning velocity	Fixed, single, or multiple passes with overlapping
Spot geometry	Circular, elliptical, rectangular
Characterization tests	OM/SEM, macro/micro hardness, GDOES, XRD, wear/erosion resistance, residual stresses

Table 2 summarizes the main differences and challenges that LST poses for every reviewed as-cast iron. It is apparent that each material presents different limitations to the extent of LST; therefore, the laser parameters and conditions must be carefully selected to fulfill the technical requirements. In the following sections, a detailed review of the characterization and results of LST in cast irons is performed to delve into the differences and advantages of the technique as a function of the initial composition.

Table 2. Comparison of LST challenges for each iron casting.

Cast Iron	Main Challenges
GI	Graphite flakes act as stress raisers in sliding or rolling contact systems; Limited improvement in wear resistance.
ADI	Susceptible to tempering effect and crack propagation in LSM; Extended costs and processing time, due to pre-austempering stage.
Pearlitic DI	Matrix carbon enrichment during heat transfer lowers the melting point around graphite nodules and produces local melting; Reduced processing window for hardening without melting.
Ferritic DI	A lesser amount of pearlite further triggers local melting around graphite nodules; LSM cannot be avoided for significant hardened case depths (>250 μm); Wear resistance is commonly lower than pearlitic DIs under similar operating conditions.

4. Laser Surface Treatment of Gray Cast Irons

LST on GIs date back to the beginnings of this technology. CO₂ lasers are the most used for this purpose, but it is frequently necessary to apply thin coatings to increase absorptivity. The characterization of this technique is carried out mainly in terms of microstructure, hardness, and wear/erosion resistance, and the relevance of each work resides in the variation of some inputs of LST or the exploration of new approaches and tests for further understanding of the process.

Regarding the microstructural changes, when the laser parameters are sufficient to ensure reaching the solid-state transformation temperature without surpassing the melting temperature, it is reported that a martensitic structure is obtained from the fast cooling of the austenitic matrix. Hwang et al. [40] used a 5 kW CO₂ laser with fixed parameters, ranging from 1 to 4.5 kW and from 1 to 13 m/min, to modify the properties of as-cast GI samples with pearlite matrix and small amounts of cementite and steadite (iron phosphite, cementite, and ferrite). The purpose of their work was the improvement of the performance of GI piston rings used in marine diesel engines by LSH, and from the experimental results, the authors determined a proper heat input window from 30 to 45 J/mm to achieve the desired hardening effect.

This conclusion is supported by Liu and Previtali [41], as the authors agree that the feasibility window for hardening without melting (LSH) is very narrow since the melting point of cast irons is lower than in pure iron or steels. In this work, a Gaussian distribution diode laser with higher absorptivity was used, and two constant temperature levels were set on the surface of the samples (1000 and 1100 °C), varying the laser power using a proportional–derivative–integrative (PID) controller, to avoid the melting of the material during heating.

Furthermore, Wang et al. [42,43] compared the effects of LSH on five types of GIs: untreated (GI), quench-tempered (QTGI), austempered (AGI), quench-tempered and laser-hardened (LHQTGI), and laser-hardened austempered (LHAGI) samples. A continuous-wave Nd: YAG laser with Gaussian energy profile and 8 ms pulse duration was used, considering a 2 mm spacing between adjacent laser spots. Three similar zones were observed in the laser-treated cases: a central laser-hardened zone, where graphite flakes completely dissolve during heating and transform to a ledeburitic matrix; a heat-affected zone (HAZ) consisting of martensite, due to self-quenching, without changes in graphite morphology; and a typical substrate microstructure of tempered martensite below the HAZ. Figure 3 presents the microstructural transformations of LHQTGI as a function of the tempering temperature.

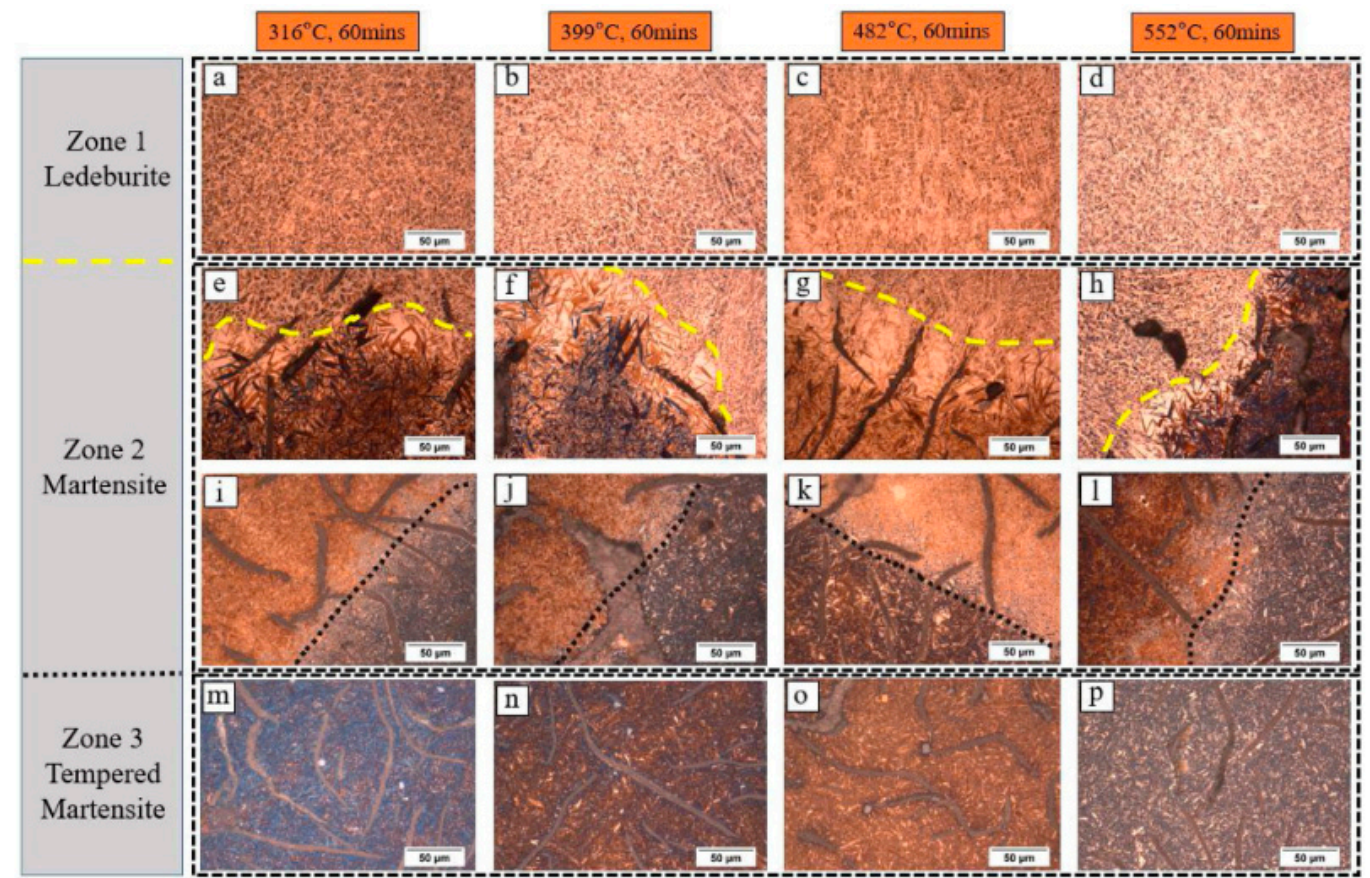


Figure 3. Microstructure of LHQTGI with different tempering temperatures: (a) laser hardened zone (Zone 1) at 316 °C, (b) Zone 1 at 399 °C, (c) Zone 1 at 482 °C, (d) Zone 1 at 552 °C, (e) interface between Zone 1 and Zone 2 (heat-affected zone) at 316 °C, (f) interface between Zone 1 and Zone 2 at 399 °C, (g) interface between Zone 1 and Zone 2 at 482 °C, (h) interface between Zone 1 and Zone 2 at 552 °C, (i) interface between Zone 2 and Zone 3 (substrate) at 316 °C, (j) interface between Zone 2 and Zone 3 at 399 °C, (k) interface between Zone 2 and Zone 3 at 482 °C, (l) interface between Zone 2 and Zone 3 at 552 °C, (m) Zone 3 at 316 °C, (n) Zone 3 at 399 °C, (o) Zone 3 at 482 °C, (p) Zone 3 at 552 °C (Reprinted with permission from ref. [43]. 2020 Elsevier).

On the other hand, Trafford et al. [44] made the first approach to LSM in GIs with different sets of fixed laser power and scanning velocity, established to ensure three different cases on the surface: hardening without fusion, with an incipient degree of fusion, and one with complete fusion on the laser path. In the case of LSM, three differentiated regions can be seen along the cross-section of the laser path: a fusion zone close to the surface, characterized by a fine ledeburite structure, which is caused by the rapid rate solidification of graphite sheets completely dissolved during heating; a deeper transition region, formed by a matrix composed of retained austenite and thick martensite plates, in which there is a partial degree of undissolved graphite sheets surrounded by a layer of ledeburite; and a base zone, where the action of the laser is not enough to produce the phase transformation. The authors also observed that cracks formed on the surface, with increased number and size according to the degree of fusion.

De Oliveira [45] also implemented a computer interface to control the temperature at the surface of GI samples, to ensure the transformation to austenite without melting, by linearly changing the heat input of a 2 kW Nd:YAG laser. However, this could not be fully achieved near the center of the laser spot, as three zones were identified by using microscopic observation: a melting zone next to the surface, with an arrange of needle-like martensite plates; a transformed region, in which graphite flakes remain unaltered and

the pearlite matrix transforms to austenite during heating, and then to larger martensite plates after the cooling process; and the substrate material zone, where no transformation was observed. The author also highlighted the difference between the shape of martensite plates, due to the high thermal conductivity of the nearby graphite flakes and the amount of diffused carbon into austenite. Moreover, a continuous heating transformation (CHT) diagram was described to explain these transformations as a function of temperature and heating rates.

In terms of mechanical properties, the hardening effect is mostly measured with Vickers microhardness tests. Hwang et al. [40] reported an increment in the hardness from about 300 to 800–950 HV0.1 in the heat-affected zone. This satisfied the piston rings requirement of the minimum hardness of 450 HV0.1 in an effective depth of 300 μm . A tempering effect was also identified in overlapping zones, where hardness dropped to 470 HV0.1, still fulfilling the desired condition.

These results are in agreement with the work of Liu and Previtali [41]. A region of maximum hardness between 800 and 900 HV0.3 was generated in the non-overlapping area, while in the overlapping region, there was a tempering effect which reduced the hardness to 300–400 HV0.3 (Figure 4). Since overlapping is used to create a homogeneous modified surface in the case of a Gaussian laser, this unwanted effect is unavoidable. In this sense, the authors determined that an overlapping degree between 1 and 1.25 mm was acceptable to comply with industrial requirements, and this, based on their research, equaled a transformed zone with a minimum depth of 0.25 mm and hardness greater than 700 HV0.3. Wang et al. [42,43] also obtained similar hardness profiles with a Rockwell test (HRC), since the 2 mm spacing between adjacent laser tracks ensured avoiding the back-tempering effect.

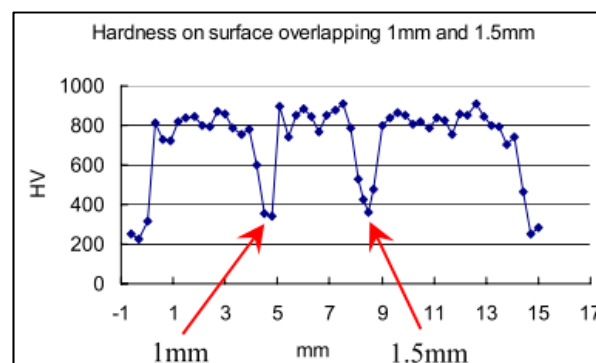


Figure 4. Microhardness profile as a function of overlapping size (Reprinted with permission from ref. [41]. 2010 Elsevier).

In the case of LSM, the improvement in hardness is comparable to LSH, but with a different magnitude. Trafford et al. [44] measured a maximum hardness of 850 HV0.3 for laser surface hardening without melting, and 950 HV0.3 for the LSM treatment. These values were reached in regions close to the surface, where the transformation is homogeneous, while hardness rapidly decays to the base value when the heat-affected zone (HAZ) is exceeded. De Oliveira [45] found a similar trend but with higher dispersion. The average hardness increased from 250 to about 600–900 HV, and the high variation was attributed to the randomness of the indentation location. Moreover, the higher hardness values were related to a higher content of martensite, as proved by X-ray diffraction (XRD) tests.

Concerning the improvement in wear resistance of GIs, Hwang et al. [40] first applied a pin-on-disc test under ASTM G99 conditions to evaluate the wear loss in both the pin (using LSH and untreated GI samples) and a conventional cast-iron disc. It was determined that LSH can double the wear life of the piston rings, which was supported with SEM observation to address the nature of the wear mechanisms. In untreated piston rings, adhesive wear features, such as plastic flow and tearing damage, were noted, while in

laser-modified samples, only mild wear was observed around the remaining graphite flakes that acted as stress raisers.

Instead, Wang et al. [42,43] conducted ball-on-plate reciprocating sliding wear tests with a hard 4 mm-diameter alumina ball (45 HRC and surface roughness of 10 nm). Both laser-hardened specimens exhibited significantly lower mass loss, since they bared harder surfaces, with LHAGI displaying better performance (Figure 5). The worn surface of laser-treated cast irons revealed a polishing effect of the ceramic ball, while the severe damage in untreated specimens was related to the stress concentration around graphite flakes and the low fracture toughness of tempered martensite (zone 3), as in Hwang et al. [40]. The main wear mechanism was crack formation (Figure 6), which surged around the edge of graphite flakes on the surface or subsurface. Then, these cracks propagated along with the graphite flakes, conceiving either small-scale pits or large-scale spalls. From these observations, the authors suggested the possibility of using LHQTGI as a replacement for AGI, since its overall performance was enhanced, and the cost and energy consumption could be substantially reduced.

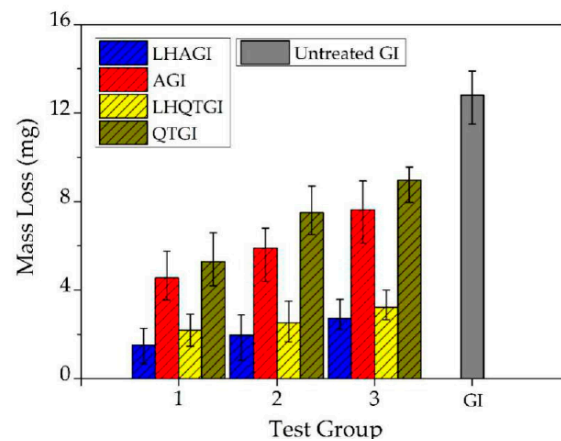


Figure 5. Mass loss of GI specimens after complete sliding wear test (Reprinted from ref. [42]).

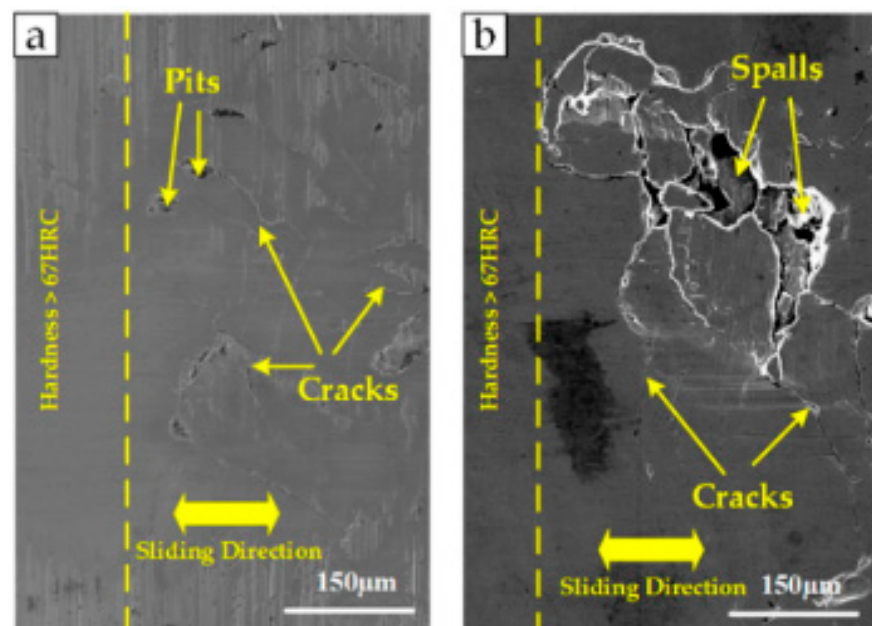


Figure 6. Worn surfaces of LHAGI and LHQTGI samples with different tempering temperatures: (a) 232 °C and (b) 316 °C (Reprinted from ref. [42]).

Trafford et al. [44] also compared the enhancement in wear resistance by LSH and LSM, using friction wear tests with a silicon carbide (SiC) platform, at a frequency of 2.5 Hz and a load of 5 kg, without lubrication. Wear rates, expressed as the amount of lost volume as a function of the total sliding distance and applied load, revealed that both LSH- and LSM-treated samples had higher resistance compared to the as-cast state, with less wear damage in the ledeburitic structure obtained by LSM.

As a summarizing work, Paczkowska [46] performed LST treatments by using various sets of laser powers and scanning velocities to determine the ranges of the surface energy density and interaction time that allowed the researcher to achieve different applications of the laser, such as tempering, hardening from the solid-state (LSH), fusion (LSM), or alloying. From the microscopic observation, as well as the measurements of temperature and hardness on the surface of the samples, the author defined the desired ranges based on a continuous wave CO₂ laser, as reported in Figure 7, highlighting how limited the processing windows are and the importance of finding the optimal laser parameters for each case.

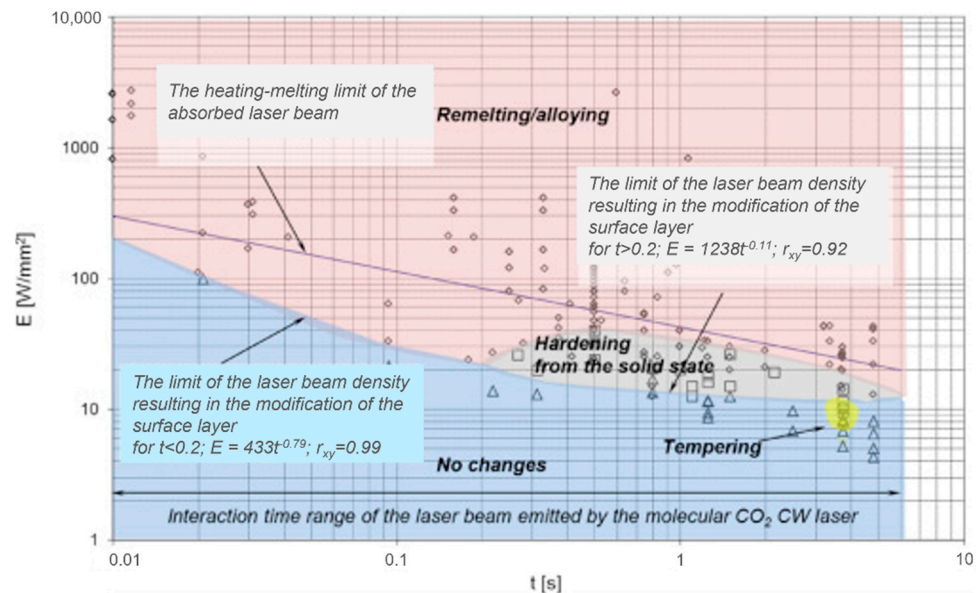


Figure 7. Energy density ranges for different heat treatments with CO₂ lasers on GI (Reprinted with permission from ref. [46]. 2016 Elsevier).

5. Laser Surface Treatment of Ductile Irons

LST on DIs has been also studied over the last decades to a similar extent, sharing the same transition between CO₂ to solid-state lasers, as well as most of the characterization tools with gray irons. However, the results indicate a strong dependence on the initial metallic matrix (e.g., pearlite or ferrite), which is responsible for the magnitude of diffusion times and cooling rates that play a major role in achieving LSH or LSM for a fixed laser input. Moreover, as Steen and Mazumder [39] proposed, many authors have verified the difficulties of achieving LSH on DIs due to the lowering of the melting point around the graphite nodules as carbon diffuses away from the graphite during the process.

5.1. Pearlitic Ductile Irons

One of the first works in the context of pearlitic DIs was carried out by Mathur and Molian [47]. The authors applied an LST treatment with a Gaussian CO₂ laser on both gray and ductile iron samples. The latter, named ASTM class 80-55-06, had a matrix with approximately 50% of pearlite. Three power levels (0.4, 0.8, and 1.2 kW) were defined, coupled with scanning velocities ranging from 4.2 to 169.3 mm/s. In addition, a manganese phosphate coating was used to increase the absorptivity of the material. The ductile iron changed its microstructure, initially pearlitic with graphite nodules surrounded by

ferritic shells to one made up of two well-defined areas. The closest zone to the surface was identified as the fusion zone, where graphite nodules completely dissolved and solidified to give rise to a martensitic-like structure, while the HAZ was evidenced by graphite nodules surrounded by martensite rings. Furthermore, in the cross-sections to the laser passing direction, the shape of the transformed zone was parabolic, similar to the original laser distribution. In addition, the researchers qualitatively determined, from several attempts to fit the experimental data, the relationship between the variables of the experiment (laser power, diameter, and scanning velocity) and the size or depth of the transformed zone. It was concluded that the reached depth was directly proportional to the power of the laser and inversely proportional to the diameter of the laser and the scanning speed.

Moreover, Molian and Mathur [48] explored the differences of applying the same treatment but changing the laser circular shape to a square and elliptical type and making single or multiple passes through the working section. The authors were able to determine a linear correlation between the depth of the transformed area and the square-shaped laser parameters considered in the term P/\sqrt{v} . On the other hand, one-dimensional (1D) and three-dimensional (3D) heat-conduction models were used to simulate the temperature on the surface of the cast iron at constant power and different scanning velocities, with sufficiently high dispersions to conclude that the thermal response of the sample to the treatment could not be described by any simplified model.

The influence of the heat input and the solidification rates was further addressed by Chen et al. [49], where a 1 mm-diameter circular CO₂ laser was used at different powers and velocities to transform the structure of a pearlitic DI. For solidification rates greater than 5×10^4 K/s, the resulting microstructure consisted of primary austenite dendrites inserted in a continuous interdendritic cementite network, while martensitic microstructures with lamellar ferrite–cementite arrays were obtained for low rates.

These transformations are consistent with the work of Gadag et al. [50], where both a CO₂ laser at different levels of constant power (1 to 2.5 kW) and a 400 W Nd:YAG laser were used, coupled with different sets of scanning velocities. In this case, three zones were identified after LSM, aided by XRD patterns: a stationary region with a homogeneous microstructure consisting mainly of ledeburite, eutectic austenite, and cementite; a slowly decreasing section below the melting zone, with martensitic and fine pearlitic microstructure; and a rapid transition to the as-cast state. Moreover, a numerical simulation of the temperature during the treatment and the cooling rate at different locations was performed based on a 3D model of the heat equation that is written as follows:

$$\rho C_p \left(\frac{\partial T}{\partial t} \right) = \nabla(k \nabla T) - U \rho C_p \left(\frac{\partial T}{\partial x} \right), \quad (2)$$

where T represents the temperature, t is the time, ρ is the density of the material, C_p is the specific heat for ductile iron, k is its thermal conductivity, and U is the constant laser scanning velocity. The finite-difference solution for the temperature at different depths was determined as a function of time. With this dataset, a successful comparison with the experimental HAZ depth was achieved, both for its magnitude and parabolic shape, thus validating the considered model.

Fernández-Vicente et al. [51] focused on the formation of cracks during the application of LSH and LSM treatments on pearlitic and bainitic DI castings used in the production of hot industrial rolls. A surface energy density of 60 J/mm² was experimentally found to be the transition between LSH and LSM treatments, using scanning velocities from 2 to 14 mm/s and powers between 2.5 and 4.4 kW. Visible cracks were observed on the samples, as illustrated in Figure 8. Only for the lowest energy density LSH, the transformation occurred without the generation of microscopically observable cracks. The homogeneous structure of the fusion layer determined by Gadag et al. [50] was also present in this work, as evidenced by a matrix composed of primary martensite (M) dendrites, together with interdendritic cementite (C), residual blocks of retained austenite (A), plate-shaped carbides (D), and ledeburite (LD).

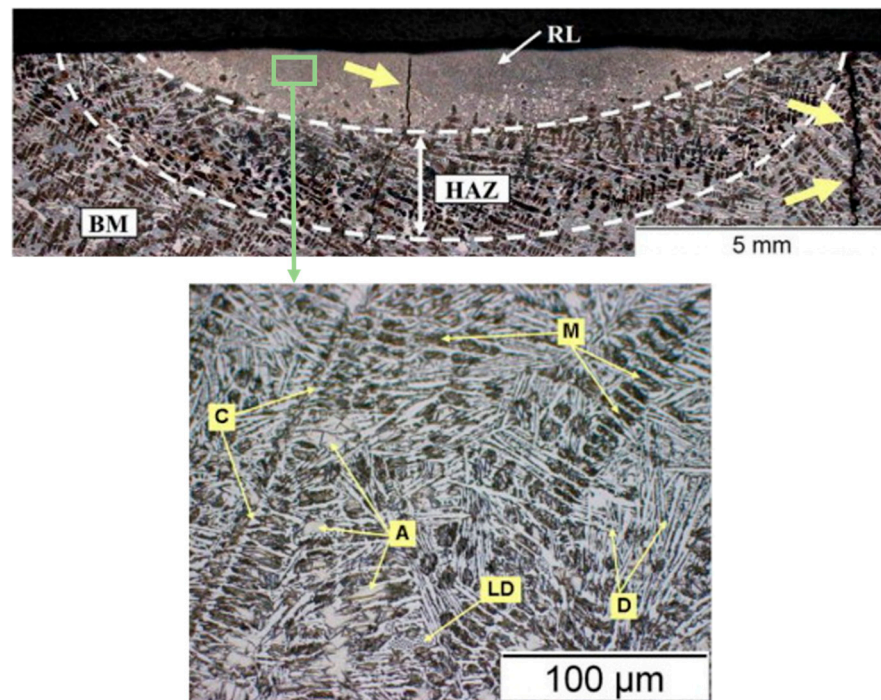


Figure 8. Microstructure of LSM ductile iron, formed by a parabolic remelted layer (RL), a heat-affected zone (HAZ), and the base material (BM), with visible cracks indicated by arrows (**top**); magnification of RL microstructure (**bottom**) (Reprinted with permission from ref. [51]. 2012 Elsevier).

A first approach on the hardening effect of LSH/LSM in pearlitic DIs was made in References [47,49], where Vickers tests were performed to measure an average hardness of 800–1000 HV in the fusion zone, compared to an original hardness between 220 and 290 HV, similar to the results found later in Molian and Baldwin [52]. However, the authors emphasized the difficulty of obtaining generalizable values in the HAZ, due to the influence of graphite nodules and their heterogeneous location in the microstructure. Moreover, in Reference [48], the effect of overlapping reported in References [40,41] for gray irons is verified for LSM.

A correlation between surface and microhardness as a function of LST parameters was also carried out by Gadag et al. [50], where it was evidenced that, the longer the interaction time (i.e., lower scanning velocities), the greater the HAZ depth. Moreover, the surface hardness increased with laser power (heat input). On the other hand, Nd:YAG produced greater surface hardness than CO₂ lasers under the same conditions, which was attributed to greater absorptivity and efficiency.

Recent investigations performed by Ghaini et al. [53] allowed us to develop a model that is able to address the absolute thermal efficiency of LSH on GGG-60 cast irons in terms of a hardening efficiency index (HEI) and a hardening ratio. A 600 W fiber laser with shielding argon gas was used at two different sets of power and four beam travel speeds to ensure a reasonable hardened area without melting. After microscopical observation and Vickers tests, the hardening efficiency index was defined as follows:

$$HEI = \frac{\Delta \text{Hardness (average)} \times \text{Hardened area}}{\text{Heat Input}}, \quad (3)$$

where the maximum achievable hardness was around 1020 HV_{0.3}, the hardened area (or volume per unit length) was obtained from the microhardness profiles and the overall transformed region in cross-section micrographs, and the heat input was measured as the ratio between beam power and laser travel speed. A linear relationship between HEI and

the term P^5/v was found, and it was compared to those of tool steels at similar operating parameters. Finally, the hardening ratio was established as follows:

$$\text{Hardening ratio} = \frac{A \times \rho \times \left(\int_{T_1}^{Ac3} C_p dT + \Delta H_a \right)}{P/v}, \quad (4)$$

where A is the area of the hardened case in cross-section, ρ is the density, T_1 is the ambient temperature, $Ac3$ is the full austenite formation temperature, C_p is the specific heat, dT is the temperature differential, and ΔH_a is the austenization enthalpy. The results were correlated with the obtained values for HEIs, and it was determined that LST with 500 W laser power and 2 mm/s travel speed achieved the maximum thermal efficiency of 15.3%.

The wear mechanisms and resistance of laser-treated pearlitic DIs were initially evaluated by Chen et al. [54], based on their previous treatments [49]. From surface erosion, abrasion, and scratch tests, it was revealed that the rate of material loss from the laser-treated bodies was reduced by a factor of up to four times, depending on the surface hardness. Subsequently, transmission electron microscopy (TEM) and scanning electron microscopy (SEM) allowed them to conclude that, for continuous high applied loads, severe plastic deformation on the surface of the treated samples generated a state of internal stresses that was responsible for the growth of microcracks that propagated, favoring the wear rate of the material.

Gadag and Srinivasan [55] also provided evidence of the improvement in the behavior of DIs treated with LSM against cavitation erosion. The authors used three classes: a pearlitic type (600/3 class), a ferritic one (400/12 class), and a 600/3 DI treated with LSM. The researchers compared the corrosion resistance in different environments, and the rate of material loss was measured from observation by optical microscopy (OM) and SEM. For the erosion tests, the three samples were exposed to artificial seawater. A linear relationship between corrosion wear and exposure time was identified, while LSM reduced the erosion rate between 6 and 8 times compared to the as-cast specimens. This improvement was attributed to the transformation of the material into a finer grain structure (consisting of ledeburite in the melting region and martensite in the hardened area) with a uniform distribution of plastic deformations and a reduction in the free path for movement of dislocations.

Molian and Baldwin [52] suggested that the improvement in erosion resistance by LST could be attributed to the emergence of beneficial compressive residual stresses during the transformation to fine martensite and retained austenite microstructures. Fernández-Vicente et al. [51] further studied the nature and magnitude of both thermal and transformational stresses due to LSM. First, thermal stresses were estimated from the temperature variations during the cycle. In particular, the only contribution to the strain was the difference between the peak temperature of the heating cycle and the temperature after the irradiation ceased. These temperatures were also approximated by simplified solutions for the heat equation, and then the value of the thermal strain was measured as follows:

$$\varepsilon = (1 + \nu)\alpha\Delta T, \quad (5)$$

where ε is the thermal strain, ν is the Poisson's ratio, α is the thermal expansion coefficient, and ΔT is the temperature variation. Then, following the linear elastic theory, the thermal stresses were estimated as follows:

$$\sigma = \frac{E}{2(1 + \nu)}\varepsilon, \quad (6)$$

where E is the elastic modulus, and σ is the thermal stress. On the other hand, the authors indicated that, for higher retained austenite contents (over 40%), the observed cracking in LSM treated samples was due to an increment in the tensile stresses from the lower specific volume of retained austenite compared to martensite or bainite (Figure 9). Finally, the retention of nucleated cracks in LSH specimens was associated with the relatively high

fracture toughness of the Fe₃C carbides present in the microstructure, and this contributes to the absorption of the thermal and transformational stresses generated during the treatment.

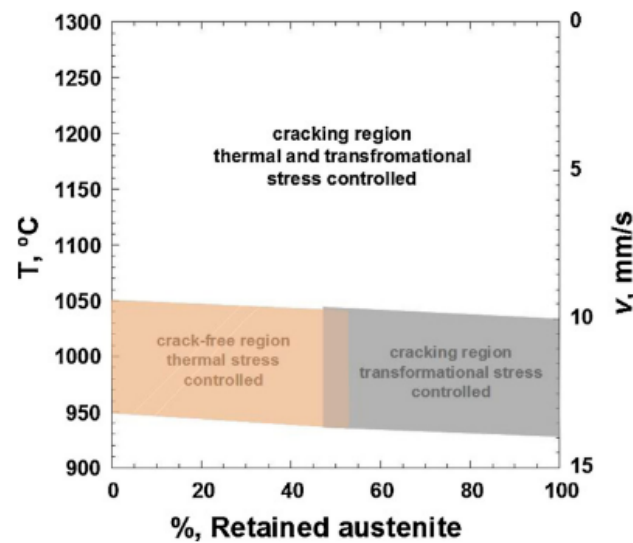


Figure 9. Laser processing window for LSH/LSM treatments as a function of retained austenite content, scanning velocity, and surface temperature (Reprinted with permission from ref. [51], 2012 Elsevier).

5.2. Austempered Ductile Irons

Since austempering produces a unique initial matrix, LST can lead to different microstructural transformations and mechanical properties. Lu and Zhang [56] first carried out LSH with a CO₂ laser on bainitic ADI samples. The material followed a standard austempering process, with an austenitizing temperature of 890 °C, a cooling interval at 360 °C for 2 h, and a final quenching to ambient conditions. The initial austenitic bainite matrix also exhibited ferrite and austenite enriched in carbon, with a smaller portion of retained austenite and martensite. After laser hardening, the matrix changed to an acicular structure of martensite and retained austenite, with graphite spots close to the surface, as seen in other ductile iron samples.

An extensive numerical model of LST in ADIs was carried out by Roy and Manna [57], with the goal to predict the temperature in the vicinity of graphite nodules. The estimation is based on the heat equation for the case of a continuous wave CO₂ laser with Gaussian distribution profile. This equation is expressed as follows:

$$\nabla^2 T - \frac{1}{\alpha} \frac{\partial T}{\partial t} + \frac{q_r}{\lambda} = 0, \quad (7)$$

where T represents the temperature, α is the thermal diffusivity, q_r is the magnitude of the heat delivered by the laser per unit volume and time, λ is the thermal conductivity, and t is the time. Assuming that heat losses are negligible and that the thermal properties of the material do not depend on the temperature, the equation was solved analytically, and the temperature profile was used to determine the magnitude of carbon diffusion away from the graphite nodules, according to Fick's law, written as follows:

$$C(y, t) = \frac{C_f - C_e}{2} \left[1 - \operatorname{erf} \left(\frac{y}{2\sqrt{Dt}} \right) \right] + C_e, \quad (8)$$

which determines the carbon concentration toward the edges of the nodule. In this expression, C_f is defined as the carbon% in the austenitic phase at the matrix–nodule interface, C_e represents the carbon concentration in the matrix, y is the measured horizontal distance from the center of the nodule (assuming a perfect circular shape), D is the diffusion coeffi-

cient (which depends on temperature), and t is the time. This carbon concentration was then utilized to define, from the iron–carbon–silicon (Fe–C–Si) phase diagram, what the temperature is when fusion occurs. Then, by selecting the proper laser parameters, this model would allow us to achieve the material hardening without melting. The authors conclude that, for laser powers below 800 W and a fixed scanning velocity of 60 mm/s, the fusion width is negligible compared to the distribution of nodules in the matrix, and, therefore, the microstructure is predominantly martensitic.

Subsequently, Roy and Manna [58] compared the results of LSH and LSM on ADI samples, using sets of parameters to ensure melting and hardening without melting. A variable laser power between 0.8 and 1.5 kW and a speed between 20 and 1000 mm/s were selected for the case of LSM, and a power between 0.5 and 1 kW and a speed of 60 mm/s were chosen for LSH analysis. The depth of the transformed zone maintained a linear relationship with the power and an inverse correlation with the scanning velocity, regardless of the chosen parameters. Microscopic observation and X-ray diffraction analysis (XRD) made it possible to determine that LSM produced a higher proportion of retained austenite in the metallic matrix, while, in LSH, martensite was the predominant phase.

Zammit et al. [59] also compared the results of implementing LSH and LSM on ADI, considering a discrete spot laser in order to avoid the reported hardness reduction in overlapping zones. A 9 kW CO₂ laser with Gaussian energy deposition profile was used to generate stationary pulses, decreasing the total energy input and, thus, producing lower distortion and processing costs. First, it was determined that melting caused severe distortion on the surface, given by an increment in surface roughness from 0.15 to 1.34 μm (in arithmetic value). Moreover, the molten region was depleted of graphite nodules, forming soft phases, such as austenite and residual ferrite, along with low carbon martensite. On the other hand, LSH only increased the average surface roughness from 0.15 to 0.43 μm , while the microstructure was mainly composed of martensite with unaltered graphite nodules. Some nodules were surrounded by a bullseye ledeburitic structure, implying that the carbon diffusion lowered the melting point locally around them, as in Roy and Manna [57]. Soriano et al. [60] were then able to verify the microstructural features of LSH in ADI by using an Nd:YAG laser coupled with a PID controller to keep the temperature in the center of the laser constant at 975 °C, so that the melting point was not exceeded during the treatment, as in Liu and Previtali [41]. A hardened zone composed of coarse martensite in the near-surface, as well as a finer acicular structure below it, was distinguished, associated with the rapid solidification without melting of the material (Figure 10a). Moreover, as evidenced in Figure 10b, the mixture of retained austenite and upper and lower bainite structures below the coarse martensitic array verified the occurrence of a softer thermal cycle in this region.

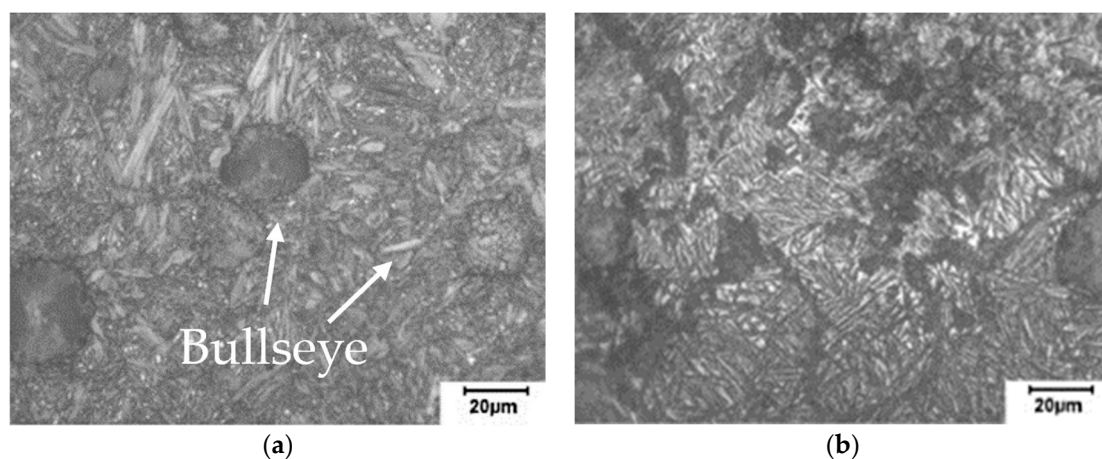


Figure 10. Micrographs of (a) top and (b) medium zones of the laser hardened ADI sample (Reprinted with permission from ref. [60]. 2011 Elsevier).

Regarding the hardening effect of the LSH, the profile as a function of depth, measured by Lu and Zhang [56], with a Knoop test with 0.2 kg load, followed the trend of the results shown in Gadag et al. [50], with a homogeneous hardness of approximately 600 KHN in the transformed zone ($\sim 250 \mu\text{m}$) and a subsequent rapid decay to the base value of the ADI specimen (300 KHN). Putatunda et al. [61] provided more evidence of the effects of LSH on the mechanical properties of ADIs. Hardness, yield stress, and ultimate tensile strength tests were conducted after initial austempering conditions similar to those of Lu and Zhang [56]. Changes in these mechanical properties were analyzed for four cases: (a) untreated ADI; samples treated with the same laser parameters, (b) initially without any type of coating; and then with two types of coating, namely (c) graphite and (d) manganese. LSH significantly increased most of the properties (except the ultimate tensile strength), obtaining the best performance under the use of coatings, since a greater energy absorption was responsible for a cooling rate that ensured the formation of a more resistant martensitic structure.

In Soriano et al. [60], the improvement of hardness was further backed up by the analysis of residual stresses (Figure 11) from XRD patterns, using the $\sin^2(\psi)$ method. The diffraction peak position of the (211) α -Fe phase was measured at nine different inclinations, ranging from -45° to 45° . The hardness of the heat-affected zone was quantified in the range of 700–800 HV, which decreased as the fraction of retained austenite increased in favor of the martensitic phase. Moreover, in the hardened region, compressive residual stresses were measured and explained by the volumetric increase associated with the transformation from austenite to harder martensite. As the depth increased, the degree of martensitic transformation decreased until the point where the matrix corresponds to the base material (0.9–1.5 mm), and, thus, the stresses become tensile. This result was also addressed by Zammit et al. [59] in their study, where it was found that compressive stresses take place near the surface, due to the 4% volumetric increase of austenite to martensite transformation. At approximately $160 \mu\text{m}$, the stresses became tensile, due to the presence of retained austenite in the ausferritic bulk, therefore obtaining an estimation of the HAZ depth of the laser treatment.

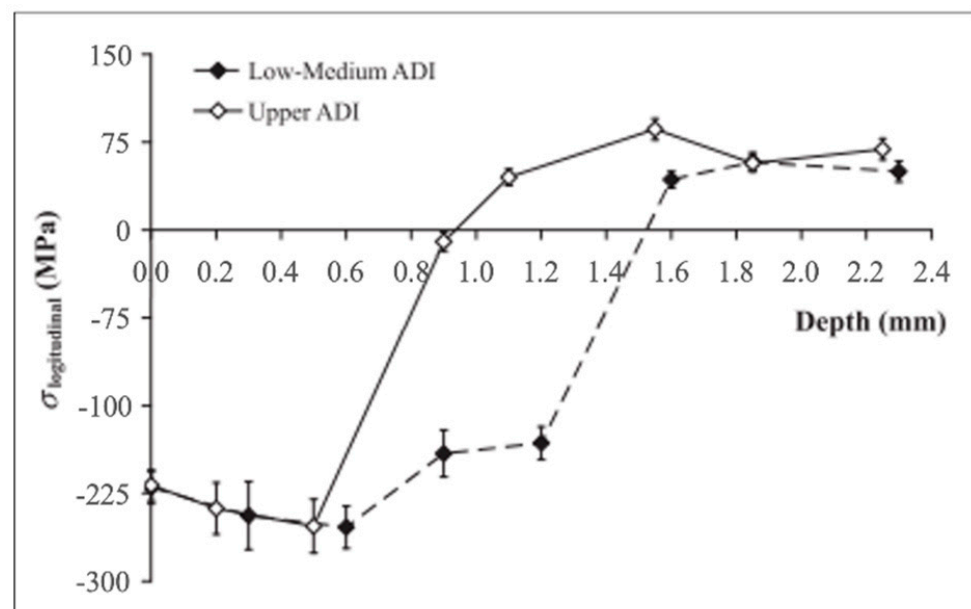


Figure 11. Evolution of residual stresses in the center of the laser track as a function of depth and ADI sample ((Reprinted with permission from ref. [60]. 2011 Elsevier).

The tribological performance of laser-modified ADIs was first assessed in Lu and Zhang [56], where the characteristics of sliding wear were analyzed from a 500-min test against a steel disc without lubrication, at a relative speed of 1.2 m/s and a variable load

between 2 and 14 kgf. The results showed a linear relationship between the mass loss due to friction and the time of the test, as in Gadag and Srinivasan [55], but it was also determined that the wear rate, in both cases, consisted of two stages: a mild one (for loads less than 10 kgf) and a severe one (for loads greater than 10 kgf). These stages were related to microstructural changes during the wear test, where the austenite phase decreased as the applied load increased. The mild phase of wear is characterized by an oxidative mechanism near the surface, while the severe phase is dominated by lamination and delamination processes, the effect of which was observed by SEM in the formation of microcracks in the surface.

Roy and Manna [58] established a relationship between the hardness profiles and the wear resistance of ADIs. The hardness distribution in LSM was parabolic, while, for LSH, it was approximately constant within the transformed zone. Thus, the presence of a more homogeneous hardened zone in LSH provided the best tribological behavior, as observed in Figure 12. For a 5 kg load, three stages in the evolution of wear were identified. Initially, a high wear rate was associated with maximum contact area. Then a stationary stage was established, due to the adherence of surface asperities originated in the first phase, to finally give way to an accelerated wear stage due, to the formation of furrows and debris separation. The optimal performance obtained by LSH is supported by a lower extent of micro-fractures that is attributed to the lower probability of causing microcracks during friction contact. This result is in agreement with the deformation restrictions at the austenite–martensite interface that are caused by changes in the residual stresses during the transformation from austenite to martensite, as detailed in References [59,60].

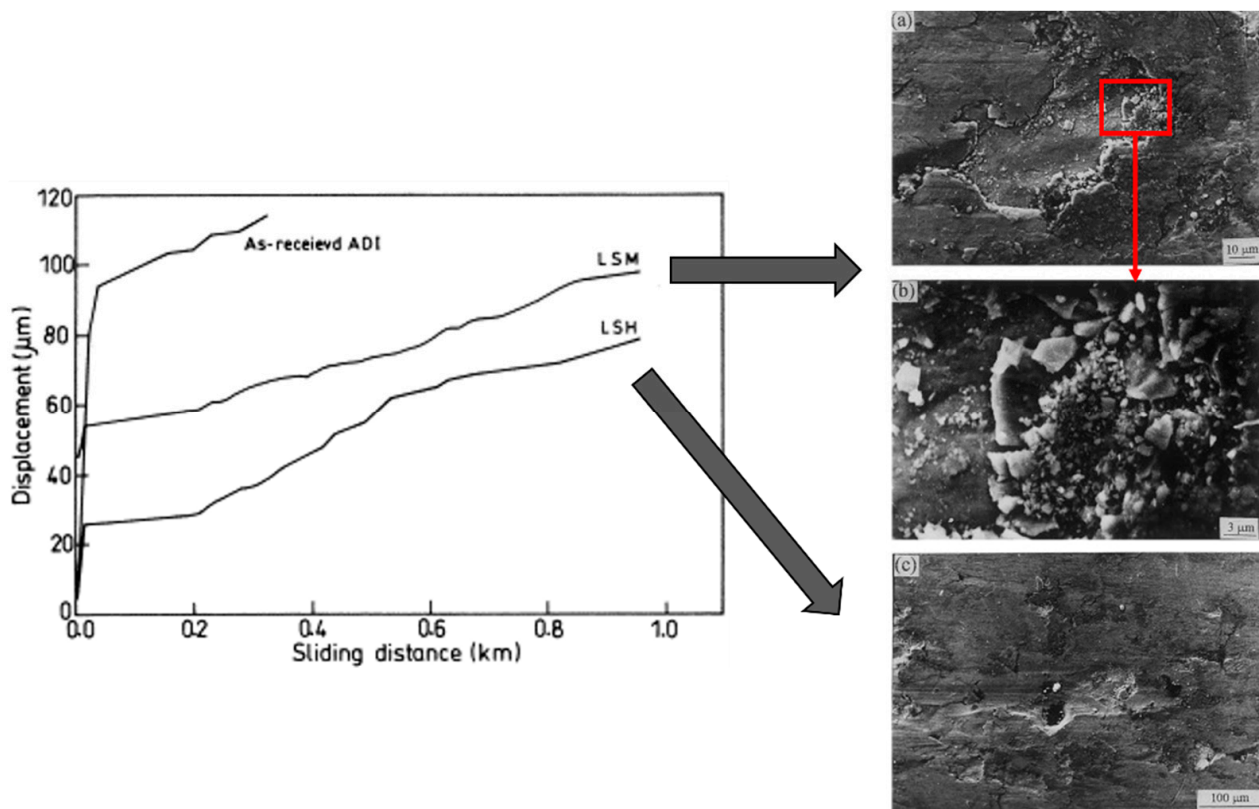


Figure 12. Evolution of displaced material as a function of sliding wear distance for as-received and laser-treated ADI samples (left); SEM micrographs of worn surfaces (right) for (a) LSM treated ADI, (b) magnified view of wear debris of (a), and (c) LSH-treated ADI (Reprinted with permission from ref. [58]. 2001 Elsevier).

The tribological characterization of LSH was completed in Zammit et al. [62]. Based on the results of Reference [59], the authors carried out discrete spot LSH treatments

by using the same CO₂ laser at 600 W and 300 ms of pulse duration and considering three different arrays: laser spots separated by one spot diameter, adjacent spots, and 50% overlapped spots. Scuffing (pin-on-disc) and rolling contact fatigue (RCF) tests were performed to address the wear resistance and mechanisms. In the first test, as-austempered and laser-treated ADI pins were considered, with a hardened and oil-lubricated AISI D2 steel counterpart disc rotating at 1450 rpm under 10 MPa constant pressure. LSH treatment with adjacent spot tracks exhibited the highest sliding cycles to failure, followed by separated spots, showing that the back-tempering effect on hardness, due to overlapping, reduced the ADI wear resistance by an order of 10–100 times. Moreover, adjacent spot LSH treatment induced a higher martensite volume fraction, which is harder than the initial microstructure and is able to delay crack initiation and propagation. On the other hand, RCF tests were performed only on as-austempered and adjacent spot laser-treated ADIs. The LSH increased the number of cycles until fatigue failure over 10⁶ times. This increment was also attributed to a harder microstructure and compressive residual stresses near the surface. It was concluded from SEM and pit observations that the main wear mechanism is governed by plastic deformation and propagation of cracks around graphite nodules, and the overall wear resistance is comparable to that of carburized steels. As a conclusion, the authors suggest that laser-treated ADIs could be suitable replacements for a variety of engineering components.

5.3. Ferritic Ductile Irons

Among all the ductile iron structures, LST in ferritic DIs has gained importance in the last decades because it lacks a significant pearlite amount (whose carbon content is higher due to the presence of cementite plates). This means that it is very difficult to find conventional ways of transforming the matrix to a martensitic type, and, on the other hand, it is difficult to achieve hardening without melting, since carbon diffusion from graphite nodules locally lowers the melting point, favoring the occurrence of melting near the surface [39].

The first modeling of the phase transformations during LST of ferritic DIs can be found in Grum and Sturm's study [63], where LSM was carried out with a low-power CO₂ laser. To ensure the fusion of the surfaces, an overlapping of 30% was considered. Three new regions arise after LSM: the melted zone, the hardened zone, and an intermediate transition zone. In the region where the liquidus temperature is exceeded, the predominantly ferritic matrix melts, and the graphite nodules diffuse toward the melted surface. This causes a strong dissolution of carbon in the liquid matrix, whose rapid solidification transforms it into austenite and ledeburite dendrites. The intermediate zone is characterized by a highly localized fusion process around the graphite nodules that, depending on the magnitude of the carbon diffusion toward their edges, can generate a ledeburite and/or martensite ring. The transformation scheme is shown in Figure 13. The differences between the transition zone and the hardened zone are that, although the matrix transforms into austenite during the heating cycle and is enriched in carbon due to diffusion away from the graphite nodules, this is not enough to locally reduce the melting point, and, therefore, the matrix becomes of martensitic type with residual austenite. In addition, due to the heterogeneous distribution of the nodules, there are areas with low carbon content where austenite reverts to ferrite during cooling.

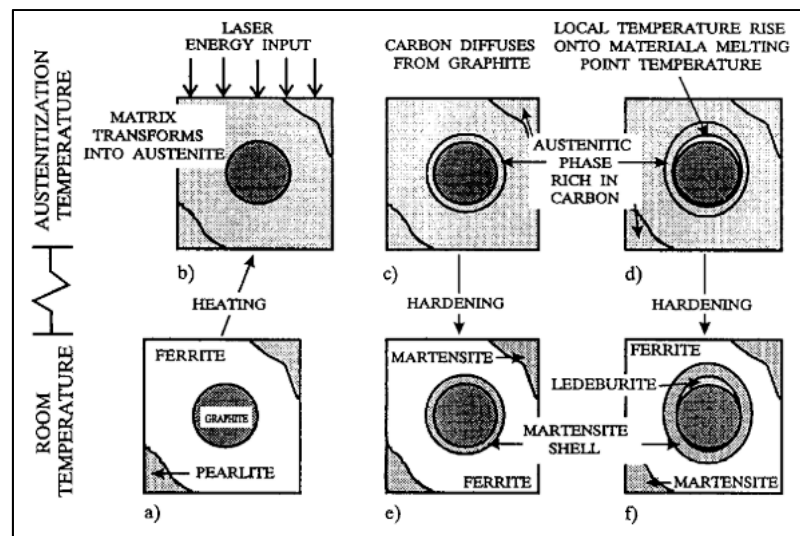


Figure 13. Schematic representation of phase changes around graphite nodules during LSM: (a) Initial DI microstructure, (b) transformation to nonhomogeneous austenite during heating, (c) carbon enrichment in austenitic matrix after diffusion, (d) local melting around graphite nodules, (e) formation of martensitic shells around graphite nodules after cooling, (f) formation of ledeburitic shells above graphite nodules that suffered local melting (Reprinted with permission from ref. [63]. 1996 Elsevier).

In Grum and Sturm [64], the analysis of LSM in ferritic DIs is completed, experimentally and numerically comparing the thickness of the martensite and ledeburite layers that surround the graphite nodules in transition and hardening zones. As described in Roy and Manna [57], from simplified models of temperature during the heating and cooling cycle, in conjunction with diffusion equations based on Fick’s law, the authors determined, at different depths, if the temperature around the nodule is enough to produce fusion (and the formation of ledeburite when cooling), in addition to calculating the magnitude of the radial diffusion of the carbon atoms. As shown in Figure 14, the simulation precisely adjusted to what was experimentally determined, which validates the use of the aforementioned models. The average standard deviation obtained is less than 10% and can be explained by model simplifications, mainly in terms of diffusion, as average values that do not vary with temperature were used.

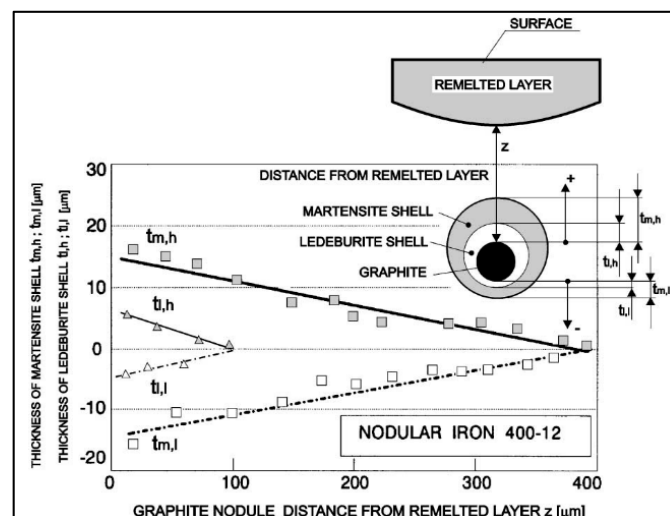


Figure 14. Comparison of the experimental and predicted thickness of martensite and ledeburite shells around graphite nodules (Reprinted with permission from ref. [64]. 2002 Elsevier).

This microstructural analysis was completed in Grum and Sturm [65], where the authors applied LSM to a similar DI sample to verify their previous models, as well as XRD and residual stress tests. The metallic surface was characterized by a high content of martensite (41%) and a portion of residual austenite (23%), and at higher depths, a reduction of the martensitic phase was observed in favor of the austenitic phase (24% and 42%, respectively, at 240 μm from the surface). From these results and the residual stresses measured at different points on the surface, it was determined that the residual austenite and martensite contents were the most influential on the nature of the internal stresses (Figure 15). The stresses on the surface always have a tensile character, since the transformations to austenitic phases involve a volume reduction of such magnitude that they cancel the effect of the transformation to martensite, thus implying a volumetric increase and, consequently, stresses of a compressive type.

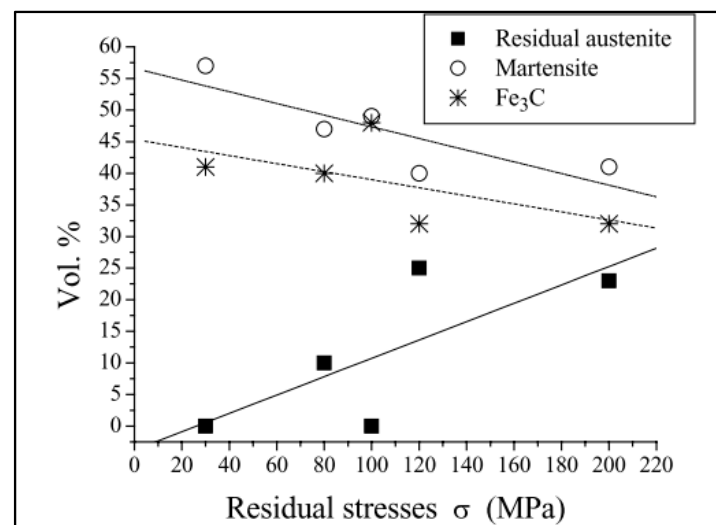


Figure 15. Evolution of residual stresses at the ductile iron surface as a function of volumetric % of phase constituents (reprinted from Reference (Reprinted with permission from ref. [65]. 2005 Inderscience Enterprises Ltd.).

Benyounis et al. [66] presented a new approach on the surface melting of DIs by conducting a comparison between the microstructural changes caused by two technologies: Nd:YAG laser and TIG. In the case of LSM, the laser was used at low power (0.1 kW) and speed of 1 mm/s with 50% overlapping, while in the case of TIG, the voltage was maintained at 50 V and the current was varied between 80 to 120 A to ensure fusion. The microstructure obtained by LSM consists of a fine dendritic structure of retained austenite, with residual percentages of martensite and cementite (Fe_3C). Although in TIG melting a dendritic structure was also observed in an austenite and cementite matrix, the main difference was the higher amount of retained austenite in LSM, which was attributed to a superior cooling rate.

The dendritic microstructure is also present in Alabeedi et al. [67], where LSM was carried out on an 83% ferrite, 11% pearlite, and 6% graphite ductile iron. A Gaussian distribution CO_2 laser was used at 3 kW power, with a scanning velocity of 10 mm/s. To achieve melting, a 50% overlapping was considered, and argon shielding gas was applied to also prevent oxidation and contamination of the specimen. The obtained microstructure was identified by SEM as austenite dendrites immersed in a cementite network, attributed to the high cooling rate during solidification. An additional transition region was observed below the melted zone; it was formed by a mixture of dendrites and thick martensite plates and added to some undissolved nodules surrounded by ledeburite layers.

Recent studies have further supported these results; for instance, Pagano et al. [68] carried out a complete analysis of the effects of the LSM technique on a ferritic DI, using an

Nd:YAG laser operating at 1 kW of power, with circular spot and Gaussian distribution. A parabolic transformed cross-section was obtained, coinciding with the laser distribution. In the area where fusion occurred, the microstructure became a network of austenite and ledeburite dendrites, with a small portion of martensite. Then a transition region with localized fusion was observed around the graphite nodules that did not melt. Finally, a hardened area was appreciated, where the graphite spheres are surrounded by a layer of martensite and immersed in a matrix of ferrite and residual austenite. These results corroborate the work of Grum and Sturm [63,64].

Another approach for LSH/LSM was conducted by Catalán et al. [69], where a fiber delivery diode laser with uniform energy distribution and rectangular shape was used. Two linear power ramps, along with two scanning velocities, were defined to achieve four different sets of linear energy densities in order to establish a relationship between the experimental results and the joint effect of all laser parameters, as well as to determine the transition between hardening from solid-state and melting. It was concluded that, for high-velocity settings (1000 mm/min), microstructural changes were not significant, whereas, for low-velocity cases (570 mm/min), severe changes could be observed. The melted zone depth increased directly proportional with the average linear energy (Figure 16), correlating with changes in the linear energy absorbed by the material and the thermal diffusion properties of the surface-modified samples. The chemical composition, as determined by GDOES, was strongly affected by the laser, with a significant increase for C and decrease for Si compared to the as-cast sample, due to the transformation of graphite nodules to carbides during the heating process. Regarding input parameters, at low energies, a Fe_3C phase was detected by XRD, whereas $\gamma\text{-Fe}_2\text{O}_3$ was raised at high energy densities, suggesting that surface oxidation occurred during the heating cycle.

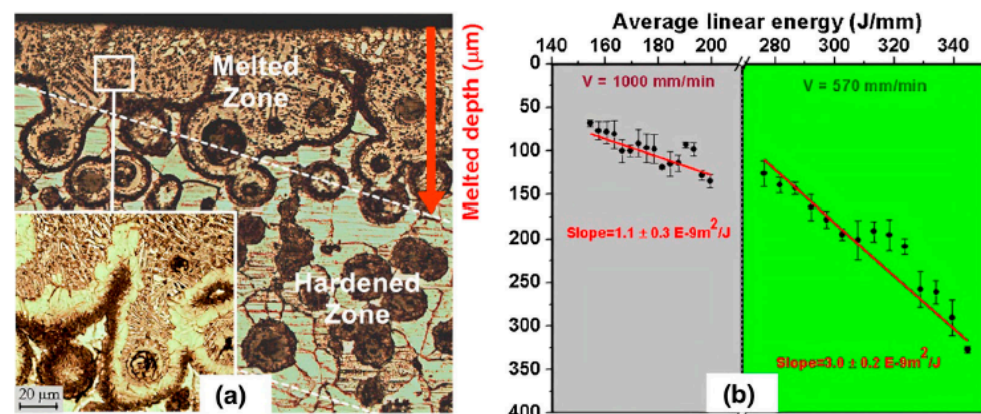


Figure 16. (a) Melted zone (MZ) and hardened zone (HZ) of laser surface-modified microstructure of DI; (b) melted depth as a function of the average linear energy of the laser (Reprinted with permission from ref. [69]. 2021 Springer Nature BV).

On the subject of hardness improvement, many of the reviewed works have quantitatively addressed the efficiency of LSM in DIs. For instance, Grum and Sturm [63] observed a uniform hardness distribution throughout the transformed layer (800–900 HV0.1), and when the limit of the hardened zone ($\approx 550 \mu\text{m}$) was exceeded, it fell rapidly to the base value (around 250 HV0.1), and this is in agreement with the posterior measurements of Pagano et al. [68]. Benyounis et al. obtained a harder microstructure when using TIG melting over LSM (750 and 500–600 HV, respectively), since the supplied energy and the interaction time ensured less retained austenite content, implying that the tempering effect of melting was reduced.

In the melted zone, Catalán et al. [69] found a stable microhardness of 1000–1100 HV0.3, which was five times higher than the nominal value. This was attributed to the carbide/oxide formation in the transformed matrix, as observed in Figure 17, since the mentioned XRD analysis supported the existence of these harder phases. The main difference

with other works is the uniformity in both hardness measurements and microstructure for the melted and hardened zones, since the laser energy distribution was uniform and rectangular shaped. Thus, overlapping of laser tracks was not needed and the tempering effect was avoided.

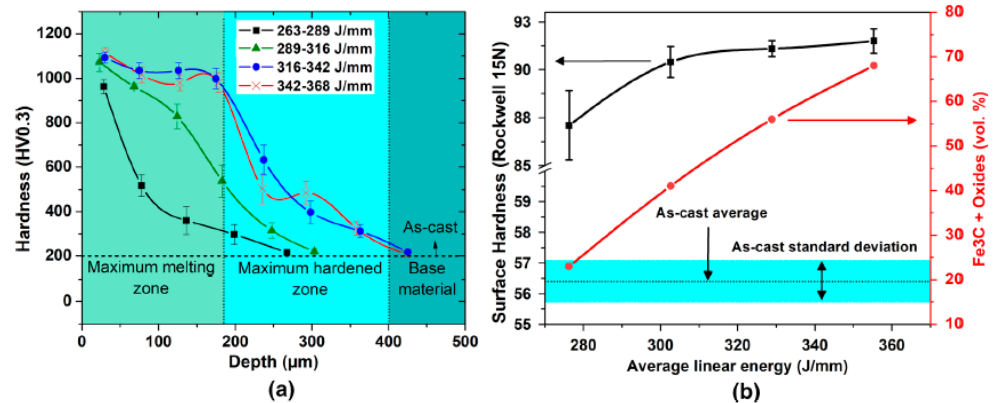


Figure 17. (a) Evolution of microhardness as a function of depth and linear energy. (b) Surface hardness and composition of as-cast and laser modified DIs (Reprinted with permission from ref. [69]. 2021 Springer Nature B.V.).

The wear response of laser melted DIs is broadly detailed in Pagano et al.'s [68] study, where a rotating steel cylinder for sliding wear tests was chosen to roll against the samples before and after being treated with LSM. The evolution of the coefficient of friction and material loss was recorded as a function of the total sliding distance. In this test, two stages were observed: initially, the coefficient of friction (COF) increases linearly with the sliding distance (run-in stage), and then it decreases to a stationary value (steady-state), due to the lubricating effect of graphite release. In this phase, since there is a partial dissolution of graphite in the hardened area, an increase in the adhesive component of the COF is generated by reducing the lubricating effect. Furthermore, the presence of hard phases, such as cementite and martensite, causes an increase in the abrasive component of the COF, which accounts for doubling the friction coefficient of the untreated DI. From Archard's equation for sliding wear, we obtain the following:

$$V = K \left(\frac{F_N \cdot S}{H} \right), \quad (9)$$

the authors verified that, for the same sliding distance (S), applied load (F_N), and wear factor (K), the greater hardness (H) of the LSM sample generated a lower volumetric loss V . This was supported by the fact that the original samples showed rapid plastic deformation during the test, while the presence of oxides on the surface of the specimens modified by LSM gave evidence of a moderate tribooxidative wear regime.

Subsequently, Ceschini et al. [70] compared the tribological experiments carried out by Pagano et al. [61] for four different specimens: untreated GI (GJL300), as-cast DI (GJS400), low-energy melted DI (GJS400-LHV at 500 W), and DI treated with LSM at high energy (GJS400-HHV at 1000 W), using the same equipment and tests as the work in comparison. Due to different energy densities, the two LSM-treated DIs exhibited different surface hardness, with the GJS400-HHV being the hardest (1100 HV1, compared to 850 HV1 for the GJS400-LHV). The sample with the best performance was the GJS400-LHV, followed by the GJS400-HHV, as observed in Figure 18. In both cases, a slight tribooxidative wear regime was observed, such that the differences reside in the presence of microcracks in the HHV cast iron, associated with its greater hardness and lower toughness. Furthermore, the results showed that graphite morphology in cast irons is a major factor in wear resistance, with the lamellar graphite shape (GJL300) being the one that acts as the greatest stress concentrator, favoring nucleation and crack growth during the sliding test.

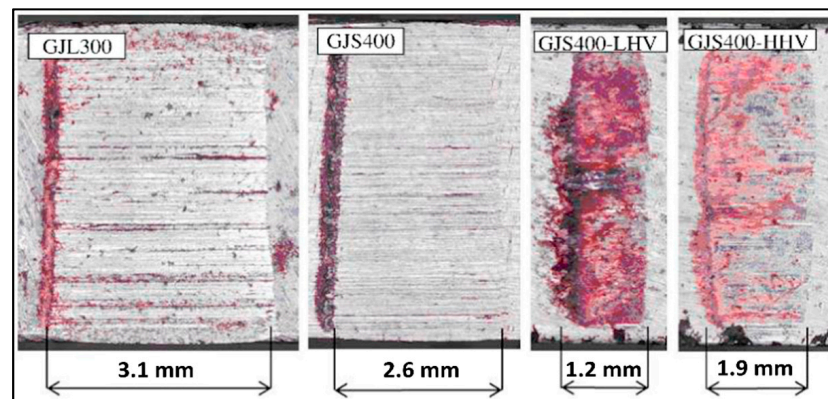


Figure 18. Worn surfaces of different cast irons for a 20 N applied load (Reprinted with permission from ref. [70]. 2016 Elsevier).

The erosion resistance enhancement due to LSM has been also assessed by Alabeedi et al. [67] in their study, where silica particles were bombarded at an average speed of 50 m/s at different incident angles. The amount of mass loss as a function of exposure time increased linearly, as in Gadag and Srinivasan [55], with a cumulative loss at the end of each trial (45 min) between 35 and 100 times less in the case of the treated samples. Furthermore, SEM examination evidenced that the wear mechanism in the untreated specimens begins with the deformation of the softer graphite nodules, which then favor the nucleation of cracks by acting as stress concentrators. Thus, the cracks form larger craters as they spread, so that the surface fractures and becomes dimpled. In contrast, wear in laser-modified samples is attributed to the initiation of fatigue cracks, which develop only into small craters. However, the hard structure formed in the process does not allow these cracks to propagate through the matrix and cause more damage, mainly due to the presence of retained austenite.

Finally, Boccardo et al. [71] developed a unidirectional coupled thermo-metallurgical model in order to predict the phase transformations of laser-treated DIs. In particular, the thermal model computed the temperature evolution during the process, while the metallurgical model predicted the phase evolution as a function of the temperature. The possible transformations during heating include the reverse eutectoid transformation (RET), homogenization of the austenite carbon content (HA), and melting transformation (MT), whereas the cooling process can comprise the eutectoid transformation (ET), solidification (ST), and martensitic transformations (MDT and MWT). To test the performance of this model, the authors considered the same DI as in Catalán et al. [69], with the four sets of linear power ramps and scanning velocities detailed in their work. Figure 19 shows the relationship between experimental and simulation results for 180 J/mm energy density. According to the presented metallurgical model, the observed thickness of the melted zone (Figure 19a) agrees with the computed temperature (Figure 19c), because it is greater than the temperature at which melting transformation ends (T_{Le}). For a depth of 100 μm , the material partially melted, because the temperature remains between the limits where melting transformation starts (T_{Ls}) and ends. Finally, for depths bigger than 300 μm , there is no phase transformation, since the temperature does not reach the point where RET starts. On the other hand, Figure 19b illustrates the evolution of the volumetric fraction of ledeburite, one of the main constituents of ductile iron during these transformations. The comparison between the computed ledeburite fraction and the thickness of melted, transition (hardened), and base material zones (Figure 19a) shows that the thermo-metallurgical model is able to identify these regions as a function of the ledeburite fraction in the transformed matrix. A linear correlation between measured and simulated martensite/ledeburite thickness layers was obtained, thus verifying that, for low thicknesses, the thermo-metallurgical model reasonably captures the trend of experimental results, and it slightly overestimates the thickness at higher magnitudes. Moreover, the thickness of the ledeburite–martensite

layer depends on the laser parameters, and it is increased with the increment of laser power and the decrement of scanning velocity.

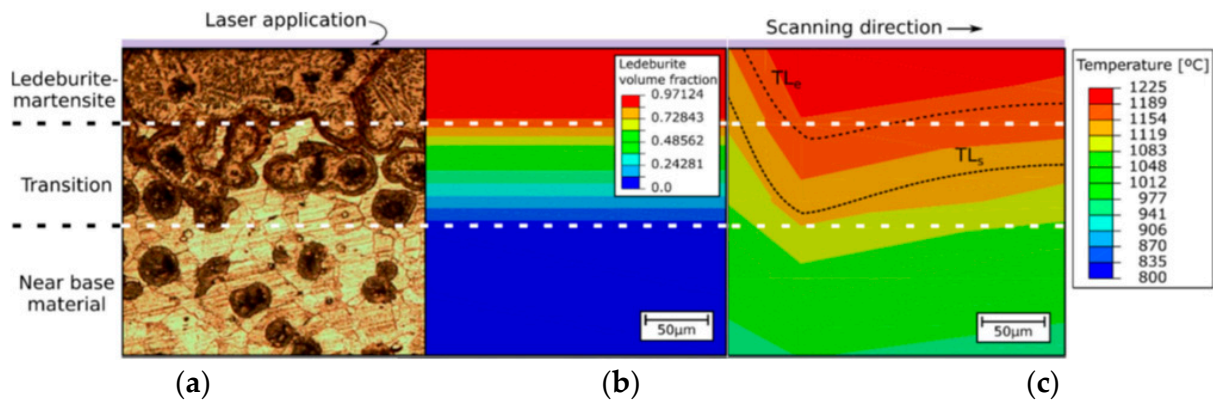


Figure 19. (a) Optical microscopy image of resulting microstructure of modified DI. (b) Computed ledeburite volume fraction at fixed laser parameters. (c) Computed temperature distribution at a fixed instant and parameters as a function of depth (Reprinted with permission from ref. [71]. 2021 Springer Nature B.V.).

5.4. Overall Facts of Surface Laser Treatment of Cast Irons

Considering the literature review, some similarities can be found in LST of cast irons, regardless of their initial microstructure. As presented in Figure 20, laser modification of iron castings generally leads to a martensitic or ledeburitic microstructure, depending on the amount of supplied energy and the subsequent phase transformations.

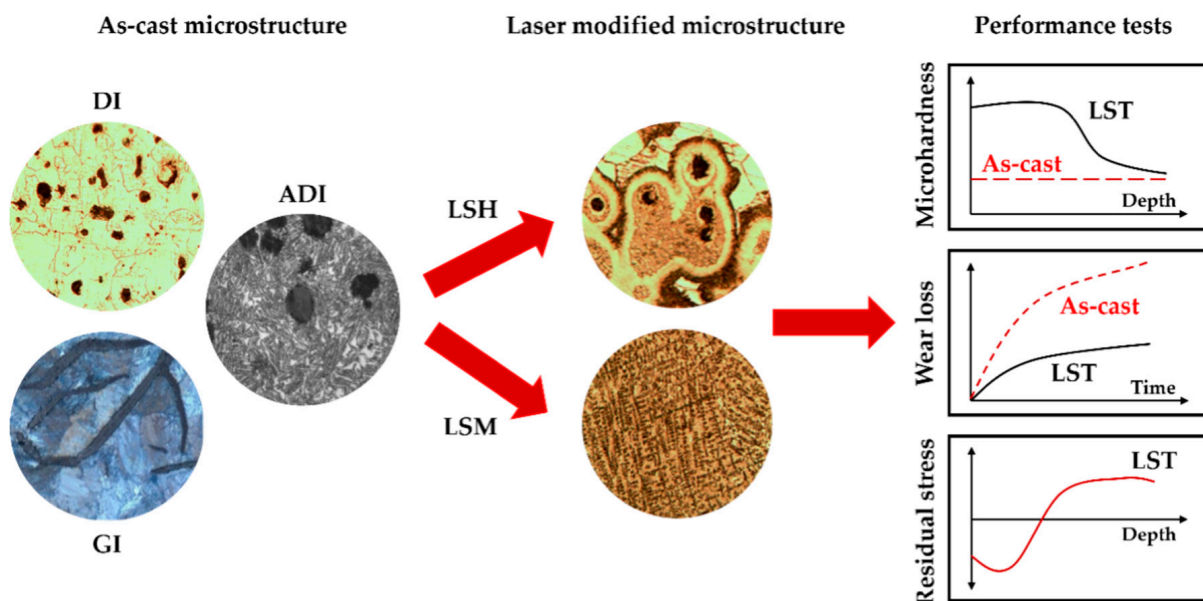


Figure 20. Summarizing diagram of microstructural transformations and overall response of laser-treated cast irons.

Moreover, mechanical/tribological characterization shows an improvement on hardness and wear resistance after LST, as explained by the formation of harder phases during rapid solidification. Microhardness curves tend to exhibit a stable, harder region, with a quasi-exponential decay to the as-cast value in zones with low degree transformation. In the case of tribological tests, mass loss is significantly reduced by both LSM and LSH; however, the wear rate is highly variable, and it depends on the conditions of the friction system. Finally, since LST encompasses volumetric transformations, the analysis of residual

stresses is important, and it usually reveals a change from compressive stresses near the surface to tensile stresses further into the as-cast region.

6. Concluding Remarks

This review highlights the evolution of the characterization of the surface thermal treatment by laser in different iron castings, divided by the main constituents and structure of their matrix. Based on what is presented in this article, LST holds numerous advantages over conventional heat treatments, as it is a precise and highly localized process for which a harder and more wear-resistant microstructure is obtained without generating a significant distortion of the workpiece. The following main conclusions can be stated:

- The use of diode and Nd:YAG lasers without coatings allows for higher absorption coefficients of the radiated energy than when using conventional CO₂ lasers.
- Lasers with circular geometry and Gaussian energy distribution generate a parabolic heat-affected zone in the transverse section, where properties are not uniform within a constant layer depth.
- Single-pass LST with rectangular-shaped and uniform energy distribution lasers, as well as adjacent discrete laser spots, can be used to avoid a tempering effect of overlapping.
- Following laser modification, DIs and ADIs present lower wear damage under comparable conditions than GIs, since graphite flakes act as stress raisers, favoring crack nucleation and growth during friction, as in dry sliding tests.
- Regardless of the initial microstructure of the cast iron, the linear energy is the key parameter, since it considers the joint effect of experimental parameters, such as laser power, absorption layer thickness, and scanning velocity. It is suggested to apply surface hardening without melting on DIs and ADIs to achieve higher wear resistance, because of the nature of the residual stresses created during phase transformations (compressive in LSH and tensile in LSM).
- Further research challenges include the analysis of the effect of alloying elements, such as Mo, Cr, or Ni, on the thermal process and mechanical properties induced by LST. Moreover, extra features, such as grain growth and surface roughness, must be added into LST simulations in order to ensure a reliable validation and determination of the scope and precision of the model.
- Future technological challenges involve the analysis of costs and implementation of LST at the industrial level, especially in high-technology and -impact environments, to evaluate the performance of this treatment in real conditions. In this regard, the information presented in this review article is a guide to encourage future investigation prospects in cast irons and ferrous alloys in general.

Author Contributions: Conceptualization, E.R.-M., A.B. and D.C.; methodology, N.C., E.R.-M. and D.C.; investigation, N.C.; writing—original draft preparation, N.C.; writing—review and editing, E.R.-M., A.B. and D.C.; visualization, E.R.-M.; supervision, E.R.-M. and D.C.; project administration, E.R.-M. and D.C.; funding acquisition, E.R.-M., A.B. and D.C. All authors have read and agreed to the published version of the manuscript.

Funding: A. Boccardo thanks the financial support received by a research grant from Science Foundation Ireland (SFI) under grant number 16/RC/3872. E. Ramos-Moore thanks FONDECYT-ANID project 1180564, and D. Celentano thanks FONDECYT-ANID project 1180591.

Institutional Review Board Statement: Not applicable.

Informed Consent Statement: Not applicable.

Data Availability Statement: Any requirement about the data of the reviewed articles must be consulted directly to the corresponding authors.

Conflicts of Interest: The authors declare no conflict of interest.

References

1. Aliakbari, K.; Masoudi Nejad, R.; Akbarpour Mamaghani, T.; Pouryamout, P.; Rahimi Asiabaraki, H. Failure analysis of ductile iron crankshaft in compact pickup truck diesel engine. *Structures* **2022**, *36*, 482–492. [[CrossRef](#)]
2. Concli, F. Austempered Ductile Iron (ADI) for gears: Contact and bending fatigue behavior. *Procedia Struct. Integr.* **2018**, *8*, 14–23. [[CrossRef](#)]
3. Artola, G.; Gallastegi, I.; Izaga, J.; Barreña, M.; Rimmer, A. Austempered Ductile Iron (ADI) Alternative Material for High-Performance Applications. *Int. J. Met.* **2016**, *11*, 131–135. [[CrossRef](#)]
4. Chakrabarty, I. *Reference Module in Materials Science and Materials Engineering*; Elsevier: Amsterdam, The Netherlands, 2018; Alloy Cast Irons and Their Engineering Applications; pp. 1–25. ISBN 978-0-12-803581-8.
5. ASM International. Casting. In *ASM Handbook*, 9th ed.; ASM International: Materials Park, OH, USA, 1998; Volume 15, pp. 1–937.
6. Collini, L.; Nicoletto, G.; Konečná, R. Microstructure and mechanical properties of pearlitic gray cast iron. *Mater. Sci. Eng. A* **2008**, *488*, 529–539. [[CrossRef](#)]
7. Jabbari Benham, M.M.; Davami, P.; Varahram, N. Effect of cooling rate on microstructure and mechanical properties of gray cast iron. *Mater. Sci. Eng. A* **2010**, *528*, 583–588. [[CrossRef](#)]
8. Willidal, T.; Bauer, W.; Schumacher, P. Stress/strain behavior and fatigue limit of grey cast iron. *Mater. Sci. Eng. A* **2005**, *413–414*, 578–582. [[CrossRef](#)]
9. Baicchi, P.; Collini, L.; Riva, E. A methodology for the fatigue design of notched castings in gray cast iron. *Eng. Fract. Mech.* **2007**, *74*, 539–548. [[CrossRef](#)]
10. Damir, A.N.; Elkhatib, A.; Nassef, G. Prediction of fatigue life using modal analysis for grey and ductile cast iron. *Int. J. Fatigue* **2007**, *29*, 499–507. [[CrossRef](#)]
11. Cueva, G.; Sinatora, A.; Guesser, W.L.; Tschiptschin, A.P. Wear resistance of cast irons used in brake disc rotors. *Wear* **2003**, *255*, 1256–1260. [[CrossRef](#)]
12. Ferrer, C.; Pascual, M.; Busquets, D.; Rayón, E. Tribological study of Fe-Cu-Cr-graphite alloy and cast iron railway brake shoes by pin-on-disc technique. *Wear* **2010**, *268*, 784–789. [[CrossRef](#)]
13. Hirasata, K.; Hayashi, K.; Inamoyo, Y. Friction and wear of several kinds of cast irons under severe sliding conditions. *Wear* **2007**, *263*, 790–800. [[CrossRef](#)]
14. Prasad, B.K. Sliding wear response of cast iron as influenced by microstructural features and test condition. *Mater. Sci. Eng. A* **2007**, *456*, 373–385. [[CrossRef](#)]
15. Prasad, B.K. Sliding wear behaviour of a cast iron as affected by test environment and applied load. *Ind. Lubr. Tribol.* **2009**, *61*, 161–172. [[CrossRef](#)]
16. Ghasemi, R.; Elmquist, L. A study on graphite extrusion phenomenon under the sliding wear response of cast iron using microindentation and microscratch techniques. *Wear* **2014**, *320*, 120–126. [[CrossRef](#)]
17. Carazo, F.D.; Giusti, S.M.; Boccardo, A.D.; Godoy, L.A. Effective properties of nodular cast iron: A multi-scale computational approach. *Comput. Mater. Sci.* **2014**, *82*, 378–390. [[CrossRef](#)]
18. Gonzaga, R.A. Influence of ferrite and pearlite content on mechanical properties of ductile cast irons. *Mater. Sci. Eng. A* **2013**, *567*, 1–8. [[CrossRef](#)]
19. Li, N.; Xing, S.; Bao, P. Microstructure and Mechanical Properties of Nodular Cast Iron Produced by Melted Metal Die Forging Process. *J. Iron Steel Res. Int.* **2013**, *20*, 58–62. [[CrossRef](#)]
20. Ceschini, L.; Morri, A.; Morri, A.; Salsi, E.; Squatrito, R.; Todaro, I.; Tomesani, L. Microstructure and mechanical properties of heavy section ductile iron castings: Experimental and numerical evaluation of effect of cooling rates. *Int. J. Cast Met. Res.* **2015**, *28*, 365–374. [[CrossRef](#)]
21. González-Martínez, R.; de la Torre, U.; Ebel, A.; Lacaze, J.; Sertucha, J. Effects of high silicon contents on graphite morphology and room temperature mechanical properties of as-cast ferritic ductile cast irons. Part II—Mechanical properties. *Mater. Sci. Eng. A* **2018**, *712*, 803–811. [[CrossRef](#)]
22. Mourujärvi, A.; Widell, K.; Saukkonen, T.; Hänninen, H. Influence of chunky graphite on mechanical and fatigue properties of heavy-section cast iron. *Fatigue Fract. Eng. Mater. Struct.* **2009**, *32*, 379–390. [[CrossRef](#)]
23. Hosdez, J.; Limodin, N.; Najjar, D.; Witz, J.-F.; Charkaluk, E.; Osmond, P.; Forré, A.; Szymtka, F. Fatigue crack growth in compacted and spheroidal graphite cast irons. *Int. J. Fatigue* **2020**, *131*, 105319. [[CrossRef](#)]
24. Iacoviello, F.; Di Cocco, V.; Bellini, C. Fatigue crack propagation and damaging micromechanisms in Ductile Cast Irons. *Int. J. Fatigue* **2019**, *124*, 48–54. [[CrossRef](#)]
25. Mohamed, I.A.; Ibraheem, A.A.; Khashaba, M.I.; Ali, W.Y. Influence of Heat Treatment on Friction and Wear of Ductile Iron: II. Role of Chromium and Nickel. *Int. J. Control Autom. Syst.* **2014**, *3*, 10–16.
26. Ben Tkaya, M.; Mezlini, S.; El Mansori, M.; Zahouani, H. On some tribological effects of graphite nodules in wear mechanism of SG cast iron: Finite element and experimental analysis. *Wear* **2009**, *267*, 535–539. [[CrossRef](#)]
27. Pintaude, G.; Bernardes, F.G.; Santos, M.M.; Sinatora, A.; Albertin, E. Mild and severe wear of steels and cast irons in sliding abrasion. *Wear* **2009**, *267*, 19–25. [[CrossRef](#)]
28. Wei, M.X.; Wang, S.Q.; Cui, X.H. Comparative research on wear characteristics of spheroidal graphite cast iron and carbon steel. *Wear* **2012**, *274–275*, 84–93. [[CrossRef](#)]

29. Panneerselvam, S.; Putatunda, S.K.; Gundlach, R.; Boileau, J. Influence of intercritical austempering on the microstructure and mechanical properties of austempered ductile iron (ADI). *Mater. Sci. Eng. A* **2017**, *694*, 72–80. [[CrossRef](#)]
30. Boccardo, A.D.; Dardati, P.M.; Celentano, D.J.; Godoy, L.A.; Górný, M.; Tyraia, E. Numerical Simulation of Austempering Heat Treatment of a Ductile Cast Iron. *Metall. Mater. Trans. B* **2016**, *47*, 566–575. [[CrossRef](#)]
31. Putatunda, S.K. Development of austempered ductile cast iron (ADI) with simultaneous high yield strength and fracture toughness by a novel two-step austempering process. *Mater. Sci. Eng. A* **2001**, *315*, 70–80. [[CrossRef](#)]
32. Putatunda, S.K.; Gadicherla, P.K. Effect of Austempering Time on Mechanical Properties of a Low Manganese Austempered Ductile Iron. *J. Mater. Eng. Perform.* **2000**, *9*, 193–203. [[CrossRef](#)]
33. Ghaderi, A.R.; Nili Ahmadabadi, M.; Ghasemi, H.M. Effect of graphite morphologies on the tribological behavior of austempered cast iron. *Wear* **2003**, *255*, 410–416. [[CrossRef](#)]
34. ASM International. Heat Treating. In *ASM Handbook*, 9th ed.; ASM International: Materials Park, OH, USA, 1998; Volume 4, pp. 1–926.
35. Li, Y.; Song, R.; Zhao, Z.; Pei, Y. Effect of three-staged normalizing on the impact wear resistance of 3.23 mass% Cr-Mn-Cu-Si cast iron. *Wear* **2019**, *426–427*, 59–67. [[CrossRef](#)]
36. Wassilkowska, A.; Dabrowski, W. Silicon as a component of ferric oxide scale covering ductile iron pipes after annealing. *Eng. Fail. Anal.* **2021**, *125*, 105381. [[CrossRef](#)]
37. Vadiraj, A.; Balachandran, G.; Kamaraj, M.; Kazuya, E. Mechanical and wear behavior of quenched and tempered alloyed hypereutectic gray cast iron. *Mater. Des.* **2011**, *32*, 2438–2443. [[CrossRef](#)]
38. Wang, B.L.; Morris, D.S.; Farshid, S.; Lortz, S.; Ma, Q.; Wang, C.; Chen, Y.; Sanders, P. Rolling contact fatigue study of chilled and quenched/tempered ductile iron compared with AISI 1080 steel. *Wear* **2021**, *478–479*, 203890. [[CrossRef](#)]
39. Steen, W.M.; Mazumder, J. *Laser Material Processing*, 4th ed.; Springer: London, UK, 2010; pp. 295–317.
40. Hwang, J.H.; Lee, Y.S.; Kim, D.Y.; Youn, J.G. Laser Surface Hardening of Gray Cast Iron Used for Piston Ring. *J. Mater. Eng. Perform.* **2002**, *11*, 294–300. [[CrossRef](#)]
41. Liu, A.; Previtali, B. Laser surface treatment of grey cast iron by high power diode laser. *Phys. Procedia* **2010**, *5*, 439–448. [[CrossRef](#)]
42. Wang, B.; Barber, G.C.; Wang, R.; Pan, Y. Comparison of Wear Performance of Austempered and Quench-Tempered Gray Cast Irons Enhanced by Laser Hardening Treatment. *Appl. Sci.* **2020**, *10*, 3049. [[CrossRef](#)]
43. Wang, B.; Pan, Y.; Liu, Y.; Lyu, N.; Barber, G.C.; Wang, R.; Cui, W.; Qiu, F.; Hu, M. Effects of quench-tempering and laser hardening treatment on wear resistance of gray cast iron. *J. Mater. Res. Technol.* **2020**, *9*, 8163–8171. [[CrossRef](#)]
44. Trafford, D.N.H.; Bell, T.; Megaw, J.H.P.C.; Brandsen, A.S. Laser treatment of grey iron. *Met. Technol.* **1983**, *10*, 69–77. [[CrossRef](#)]
45. De Oliveira, U.O.B. Laser Treatment of Alloys: Processing, Microstructure and Structural Properties. Ph.D. Thesis, University of Groningen, Groningen, The Netherlands, 2007.
46. Paczkowska, M. The evaluation of the influence of laser treatment parameters on the type of thermal effects in the surface layer microstructure of gray irons. *Opt. Laser Technol.* **2016**, *76*, 143–148. [[CrossRef](#)]
47. Mathur, A.K.; Molian, P.A. Laser Heat Treatment of Cast Irons—Optimization of Process Variables: Part I. *J. Eng. Mater. Technol.* **1985**, *107*, 200–207. [[CrossRef](#)]
48. Molian, P.A.; Mathur, A.K. Laser Heat Treatment of Cast Irons—Optimization of Process Variables: Part II. *J. Eng. Mater. Technol.* **1986**, *108*, 233–239. [[CrossRef](#)]
49. Chen, C.H.; Ju, C.P.; Rigsbee, J.M. Laser surface modification of ductile iron: Part 1 Microstructure. *Mater. Sci. Technol.* **1988**, *4*, 161–166. [[CrossRef](#)]
50. Gadag, S.P.; Srinivasan, M.N.; Mordike, B.L. Effect of laser processing parameters on the structure of ductile iron. *Mater. Sci. Eng. A* **1995**, *196*, 145–154. [[CrossRef](#)]
51. Fernández-Vicente, A.; Pellizzari, M.; Arias, J.L. Feasibility of laser surface treatment of pearlitic and bainitic ductile irons for hot rolls. *J. Mater. Processing Technol.* **2012**, *212*, 989–1002. [[CrossRef](#)]
52. Molian, P.A.; Baldwin, M. Effects of single-pass laser heat treatment on erosion behavior of cast iron. *Wear* **1987**, *118*, 319–327. [[CrossRef](#)]
53. Ghaini, F.M.; Ameri, M.H.; Torkamany, M.J. Surface transformation hardening of ductile cast iron by a 600 w fiber laser. *Optik* **2020**, *203*, 163758. [[CrossRef](#)]
54. Chen, C.H.; Ju, C.P.; Rigsbee, J.M. Laser surface modification of ductile iron: Part 2 Wear mechanism. *Mater. Sci. Technol.* **1988**, *4*, 167–172. [[CrossRef](#)]
55. Gadag, S.P.; Srinivasan, M.N. Cavitation erosion of laser-melted ductile iron. *J. Mater. Process. Technol.* **1995**, *51*, 150–163. [[CrossRef](#)]
56. Lu, G.; Zhang, H. Sliding wear characteristics of austempered ductile iron with and without laser hardening. *Wear* **1990**, *138*, 1–12.
57. Roy, A.; Manna, I. Mathematical modelling of localized melting around graphite nodules during laser surface hardening of austempered ductile iron. *Opt. Lasers Eng.* **2000**, *34*, 369–383. [[CrossRef](#)]
58. Roy, A.; Manna, I. Laser surface engineering to improve wear resistance of austempered ductile iron. *Mater. Sci. Eng. A* **2001**, *297*, 85–93. [[CrossRef](#)]
59. Zammit, A.; Abela, S.; Betts, J.C.; Grech, M. Discrete spot laser hardening of austempered ductile iron. *Surf. Coat. Technol.* **2017**, *331*, 143–152. [[CrossRef](#)]

60. Soriano, C.; Leunda, J.; Lambarri, J.; García Navas, V.; Sanz, C. Effect of laser surface hardening on the microstructure, hardness and residual stresses of austempered ductile iron grades. *Appl. Surf. Sci.* **2011**, *257*, 7101–7106. [[CrossRef](#)]
61. Putatunda, S.; Bartosiewicz, L.; Hull, R.J.; Lander, M. Laser Hardening of Austempered Ductile Iron (ADI). *Mater. Manuf. Process.* **1997**, *12*, 137–151. [[CrossRef](#)]
62. Zammit, A.; Abela, S.; Betts, J.C.; Michalczewski, R.; Kalbarczyk, M.; Grech, M. Scuffing and rolling contact fatigue resistance of discrete laser spot hardened austempered ductile iron. *Wear* **2019**, *422–423*, 100–107. [[CrossRef](#)]
63. Grum, J.; Sturm, R. Microstructure analysis of nodular iron 400-12 after laser surface melt hardening. *Mater. Charact.* **1996**, *37*, 81–88. [[CrossRef](#)]
64. Grum, J.; Sturm, R. Comparison of measured and calculated thickness of martensite and ledeburite shells around graphite nodules in the hardened layer of nodular iron after laser surface remelting. *Appl. Surf. Sci.* **2002**, *187*, 116–123. [[CrossRef](#)]
65. Grum, J.; Sturm, R. Microstructure variations in the laser surface remelted layer of nodular iron. *Int. J. Microstruct. Mater. Prop.* **2005**, *1*, 11–23. [[CrossRef](#)]
66. Benyounis, K.Y.; Fakron, O.M.A.; Abboud, J.H.; Olabi, A.G.; Hashmi, M.J.S. Surface melting of nodular cast iron by Nd-YAG laser and TIG. *J. Mater. Process. Technol.* **2005**, *170*, 127–132. [[CrossRef](#)]
67. Alabeedi, K.F.; Abboud, J.H.; Benyounis, K.Y. Microstructure and erosion resistance enhancement of nodular cast iron by laser melting. *Wear* **2009**, *266*, 925–933. [[CrossRef](#)]
68. Pagano, N.; Angelini, V.; Ceschini, L.; Campana, G. Laser remelting for enhancing tribological performances of a ductile iron. *Procedia CIRP* **2016**, *41*, 987–991. [[CrossRef](#)]
69. Catalán, N.; Ramos-Moore, E.; Boccardo, A.; Celentano, D.; Alam, N.; Walczak, M.; Gunasegaram, D. Surface Laser Treatment on Ferritic Ductile Iron: Effect of Linear Energy on Microstructure, Chemical Composition, and Hardness. *Metall. Mater. Trans. B* **2021**, *52*, 755–763. [[CrossRef](#)]
70. Ceschini, L.; Campana, G.; Pagano, N.; Angelini, V. Effect of laser surface treatment on the dry sliding behavior of the EN-GJS400-12 ductile cast iron. *Tribol. Int.* **2016**, *104*, 342–351. [[CrossRef](#)]
71. Boccardo, A.D.; Catalán, N.; Celentano, D.J.; Ramos-Moore, E. A Thermo-metallurgical Model for Laser Surface Engineering Treatment of Nodular Cast Iron. *Metall. Mater. Trans. B* **2021**, *52*, 854–870. [[CrossRef](#)]